ARTICLE

Genesis of the Taolin Pb-Zn deposit in northeastern Hunan Province, South China: constraints from trace elements and oxygen-sulfur-lead isotopes of the hydrothermal minerals

Deshui Yu[1,2] · Deru Xu[3] · Zhaoxia Zhao[1,2] · Qinyi Huang[1,2] · Zhilin Wang[4] · Teng Deng[3] · Shaohao Zou[3]

Abstract

Located in the northeastern Hunan Province of South China, the Taolin Pb-Zn deposit is one of many metallic deposits structurally controlled by extensional faults in the central segment of the Jiangnan Orogen. The deposit occurs in a tectonic breccia zone between the Mufushan pluton and the Neoproterozoic Lengjiaxi Group. Field and microscopic observations reveal that the hydrothermal ore-forming processes at Taolin can be divided into five stages, from early to late: (1) coarse-grained quartz, (2) quartz + fluorite + chlorite + claybank sphalerite (Sp1) + galena + chalcopyrite, (3) quartz + barite + pale-yellow sphalerite (Sp2) + galena + chalcopyrite, (4) quartz ± chalcopyrite, and (5) fine-grained quartz, in which the stages 2 and 3 are regarded as the main Pb-Zn-forming events. LA-ICP-MS analyses show that Sp1 has higher contents of Fe, Mn, Co, In, and Sn, but lower contents of Ge and Sb, relative to the Sp2. Trace element concentrations of the sphalerite suggest a medium-low temperature hydrothermal event dominated in the Taolin deposit and that the ore fluids gradually decreased in the estimated average temperature and became relatively oxidized from stages 2 to 3. The $\delta^{18}O$ values of ore fluids calculated from in situ analysis on the stages 2 and 3 quartz suggest the ore fluids are from a mixture of magmatic and meteoric waters. The $\delta^{34}S$ values of sulfides/sulfates from stages 2 and 3 mineralization indicate a dominating magmatic affinity for sulfur. Further, lead isotope compositions for the stages 2 and 3 sulfides are similar to those of the Mufushan pluton, indicating that the ore metals may have been derived from the latter. We thus propose that the Taolin deposit precipitated from a medium-low temperature magmatic-hydrothermal system most likely related to the Mufushan pluton.

Keywords Hydrothermal minerals · In situ analysis · O-S-Pb isotopes · Taolin Pb-Zn deposit · Northeastern Hunan Province of South China

---

Editorial handling: B. Lehmann

✉ Deru Xu
xuderu@gig.ac.cn

1 CAS Key Laboratory of Mineralogy and Metallogeny, Guangzhou Institute of Geochemistry, Chinese Academy of Sciences, Guangzhou 510640, China

2 University of Chinese Academy of Sciences, Beijing 100049, China

3 State Key Laboratory of Nuclear Resources and Environment, East China University of Technology, Nanchang 330013, China

4 School of Geosciences and Info-Physics, Central South University, Changsha 410083, China

Introduction

Vein-type Pb-Zn ± Ag deposits, as an important source of base metals, commonly have close relationships with porphyry and/or skarn systems, and have been recognized as the distal products of magmatic-hydrothermal systems (Lawley et al. 2010; Sillitoe 2010; Bonsall et al. 2011; Box et al. 2012; Catchpole et al. 2015; Li et al. 2017; Zhai et al. 2018, 2019). However, there are also some base metal veins that do not appear to be spatially and genetically linked to porphyry or skarn systems, and their genesis remains controversial (Li et al. 2013; Ma et al. 2019). Such the vein-type deposits are distinctly hydrothermal in origin, although the source of ore-forming fluids and metals may be either magmatic or non-magmatic (Kissin and Mango 2014). In most instances, both fluid and metal sources are still greatly debated (Zhai et al. 2018, 2019).

Situated between the Yangtze Block and Cathaysia Block in South China, the Jiangnan Orogen is a significant metallogenic belt hosting abundant Au-Sb-W and Cu (-polymetallic) deposits (Xu et al. 2017). Several decades ago, some Au, Cu, Pb-Zn, and Co deposits were also discovered in northeastern Hunan Province, which geotectonically is traditionally regarded as the central segment of the Jiangnan Orogen. Among these, the Taolin Pb-Zn deposit occupies a reserve of 0.98 Mt Pb+Zn, with average grades of 1.22 wt% for Pb and 1.13 wt% for Zn. Besides, the Pb-Zn orebodies are strictly controlled by detachment fault zones (Fu et al. 1991). Therefore, it is necessary to figure out the genesis of the Taolin Pb-Zn deposit, which will be in favor of exploration for potentially more Pb and Zn resources in the region.

Previous studies have mainly described the geological characteristics, host rocks, and mineral paragenesis of the Taolin deposit (Zhang and Fu 1987; Zhang 1989; Fu et al. 1991; Li and Yu 1991; Li 1992; Yu 1993; Yu et al. 1998; Yu and Ye 1998; Kang et al. 2015). However, source(s) for the ore-forming materials and fluids and the genetic affiliation of the Taolin Pb-Zn deposit have been controversial. Anyway, the Taolin deposit has been interpreted as one of the three types of ore genesis: medium-low temperature hydrothermal vein-type (Wang et al. 1981; Ding and Rees 1984; Wei and Ding 1984; Ding et al. 1986; Zou 1993; Kang et al. 2015), sedimentary-hydrothermally reworked type (Zhang and Fu 1987; Zhang 1989), or low-temperature epithermal type (Roedder and Howard 1988). As for the ore-forming materials, several sources were suggested, such as from (1) lower crust or Mesozoic granite (Wang et al. 1981; Ding and Rees 1984; Wei and Ding 1984; Ding et al. 1986; Kang et al. 2015), (2) both Neoproterozoic Lengjiaxi Group and Mesozoic granite (Yu et al. 1998), and (3) Neoproterozoic Lengjiaxi Group (Zhang and Fu 1987; Zhang 1989). Besides, two sources of ore-forming fluids were interpreted as the results of (1) mixture of magmatic water and meteoric water (Wei and Ding 1984; Ding et al. 1986; Yu et al. 1998; Kang et al. 2015), and (2) meteoric water with minor metamorphic water (Zhang and Fu 1987; Zhang 1989; Li and Yu 1991; Li 1992). However, most of those conclusions are from the evidence of separating mineral analysis, which may cause prejudice to encode the ore genesis of the Taolin deposit. Therefore, the sources of ore fluids and ore metals of the Taolin deposit should be reconsidered based on the state-of-the-art analytical methods, although this deposit has been mined for more than 60 years.

In this paper, the electron microprobe analysis (EMPA) and laser ablation inductively coupled plasma mass spectrometry (LA-ICP-MS) analyses were conducted on sphalerites from Taolin Pb-Zn deposit for obtaining the major and trace elements. Correspondingly, the substitution mechanisms of trace elements and the formation conditions of these sphalerites were discussed. In addition, the in situ oxygen and sulfur isotopes were analyzed on the quartz and sulfides/sulfate, respectively, to encode the source(s) and evolution of the ore fluids. Besides, the lead isotopic components of the sulfides and associated granites are analyzed to deduce the origin of the ore metals. Integrating the above data, we attempt to elucidate the ore-forming process(es) and to identify the genetic type of the Taolin Pb-Zn deposit.

Regional geology

South China Block (SCB) comprises the Yangtze Block to the northwest and the Cathaysia Block to the southeast (Fig. 1a), which were assembled to form the Jiangnan Orogenic Belt during Neoproterozoic (e.g., Zhou et al. 2002; Zhao and Cawood 2012; Wang et al. 2014b; Yao et al. 2014; Zhao 2015). The Jiangnan Orogenic Belt is a tectonic unit composed of low-grade metamorphic Neoproterozoic sedimentary-volcanic rocks and massive granite intrusions. It is curved across northern Guangxi, eastern Guizhou, western and northern Hunan, northern Jiangxi, southern Anhui, and northern Zhejiang (Wang et al. 2013b). In South China, four major episodes of magmatism have been recognized, including the Neoproterozoic (Jinningnian), the Early Paleozoic (Caledonian or Kwangsian), the Early Mesozoic (Indosinian), and the Late Mesozoic (Yanshanian) (Zhou et al. 2006; Zhao and Cawood 2012; Charvet 2013; Shu et al. 2015). Among these, the Late Mesozoic (180–67 Ma) magmatism initiated by the Yanshanian Orogeny is the most intensive episode (Deng et al. 2017). It has been generally accepted that the subduction and subsequent rollback of the Paleo-Pacific plate resulted in the voluminous Late Mesozoic I-S-type granitoids as well as the predominant NE-trending faults in South China (Li and Li 2007; Wang et al. 2007b; Jiang et al. 2009; Zhu et al. 2014). Amounts of A-type granitoids with the age of ca. 160 Ma were developed in the Nanling Range including part of the Jiangnan Orogenic Belt, indicating that the SCB had been in an extensional tectonic setting since ca. 160 Ma (Li et al. 2007).

Northeastern Hunan Province is located in the central segment of the Jiangnan Orogenic Belt, South China (Fig. 1a, b). The main rocks outcropped in northeastern Hunan are metasediments of the Neoproterozoic successions and Meso-Cenozoic red-bed sedimentary rocks (Fig. 1b). The Neoproterozoic successions consist of the Early to Middle Neoproterozoic (ca. 860–820 Ma; Wang et al. 2008, 2010, 2012a, 2012b, 2013b, 2014b; Zhou et al. 2009; Gao et al. 2011; Zhang et al. 2012; Zhang and Zheng 2013) Lengjiaxi Group and the Middle Neoproterozoic (ca. 815–760 Ma; Wang et al. 2007a, 2013a; Gao et al. 2011) Banxi Group, with both of them separated by the angular unconformity (Wang et al. 2007a).

The northeastern Hunan Province is characterized by the Basin-and-Range-like tectonic framework, which consists of three basins and two uplifts separated by a series of regional
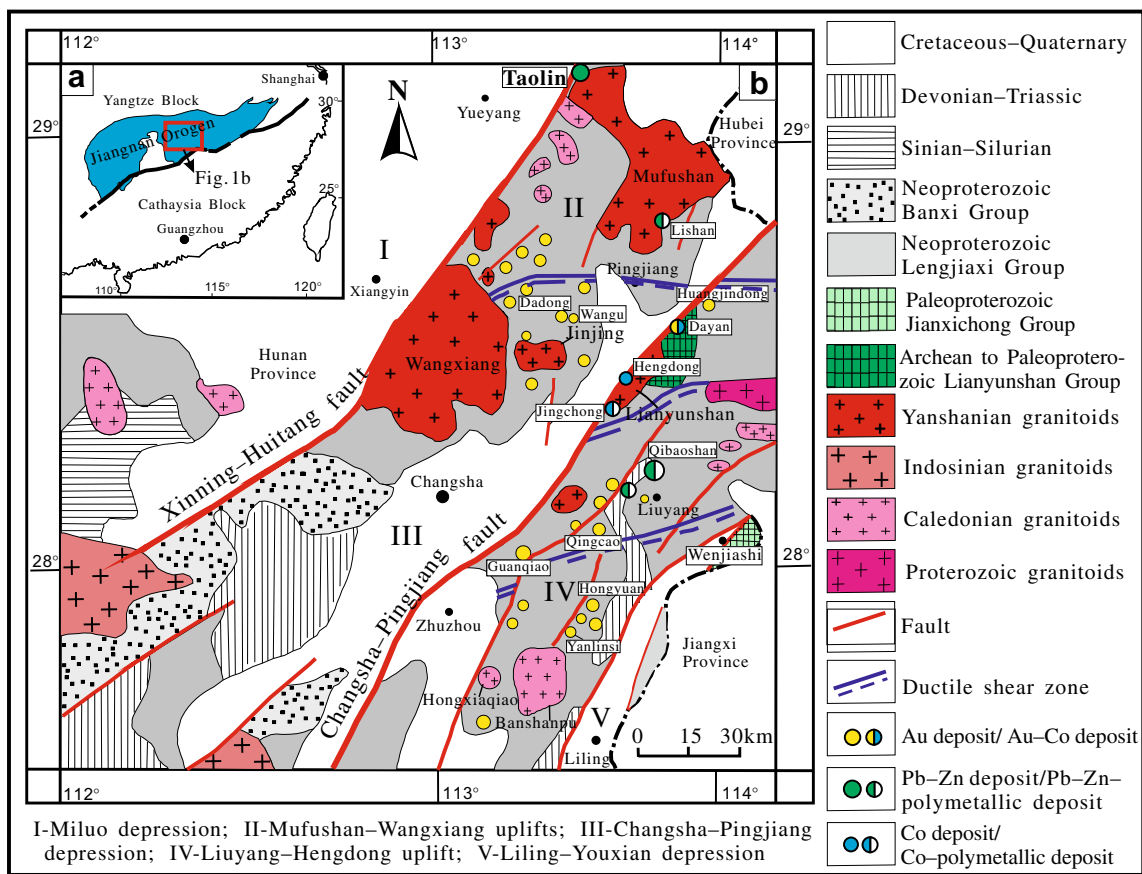
Fig. 1 **a** Simplified sketch map of South China showing the location of the Jiangnan Orogen, modified after Zhao (2015). **b** Geological map of northeastern Hunan Province showing the structures, lithologies, and magmatic rocks and different types of ore deposits, modified after Xu et al. (2009)

NE- to NNE-trending marginal faults (Fig. 1b). From NW to SE, these basins and uplifts include the Miluo graben basin, the Mufu-Wangxiang uplift, the Changsha-Pingjiang graben basin, the Liuyang-Hendong uplift, and the Liling-Youxian graben basin (Xu et al. 2009). The individual basins are largely filled by the Cretaceous red-bed clastic rocks, whereas each of the uplifts comprises Precambrian metamorphic volcaniclastic sedimentary rocks and granitoids intruded by the Late Silurian to Cretaceous granitoids. The NE- to NNE-trending crustal-scale strike-slip shear faults that are situated at the transitions between basins and uplifts are defined by a series of deep faults such as Xinning-Huitang, Changsha-Pingjiang, etc. (Fig. 1b; Fu 2009; Wen et al. 2016). Moreover, the Basin-and-Range-like tectonic framework was most likely caused by Late Mesozoic extension proposed by Xu et al. (2017). Granitoid intrusions are well-developed in the northeastern Hunan Province (Fig. 1b). The emplacement age for those granitoids include the Early to Late Neoproterozoic represented by the Getengling pluton of ca. 845 Ma ages (Deng et al. 2019), the Caledonian Banshanpu and Hongxiaqiao plutons of ca. 434–420 Ma ages (Xu et al. 2006; Guan et al. 2014; Li et al. 2015), the Yanshanian Mufushan, Wangxiang, Jinjing, and Lianyunshan plutons of

ca. 160–127 Ma ages (Jia et al. 2003; Shi et al. 2013; Wang et al. 2014a; Deng et al. 2017; Ji et al. 2017).

A number of Au-, Cu-, Co-, and Pb-Zn deposits occur in northeastern Hunan Province, and spatially have an intimate relationship with the Late Mesozoic granitoids (Fig. 1b). The representative ore deposits include the Dawan Au deposit, the Taolin Pb-Zn deposit, and the Lishan Pb-Zn polymetallic deposit in the Mufu-Wangxiang uplift, and the Huangjindong Au deposit, the Qibaoshan Cu-Pb-Zn deposit, and the Jingchong and Hengdong Co-Cu polymetallic deposits in the Liuyang-Hendong uplift (Fig. 1b). Herein, the Taolin Pb-Zn deposit is the focus of the present study.

Deposit geology

The outcropped strata in the Taolin mining district are composed of the Neoproterozoic Lengjiaxi Group, the Cretaceous Fenshuiao Formation, the Tertiary Jianjiaxi Formation, and the Quaternary cover. Both the Tertiary-Cretaceous terrigenous sediments and the Quaternary cover were deposited in the Miluo graben basin to the west of the Taolin detachment fault zone as shown in Fig. 2 a. There is an unconformity at the
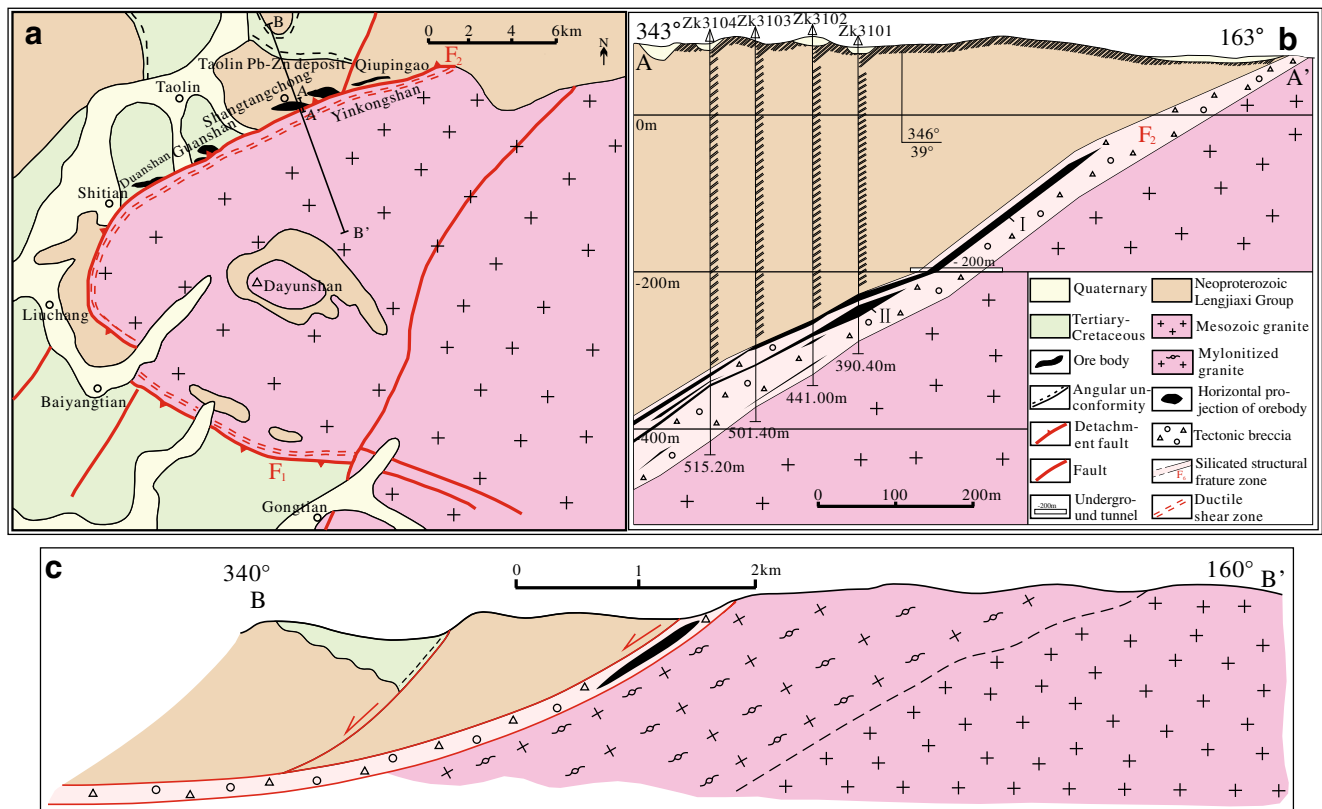
Fig. 2 a Simplified geological map of the Taolin Pb-Zn deposit, modified after Yu and Ye (1998). b The No. 31 exploration line profile along line A–A' of the Taolin deposit. c A schematic cross section along line B–B' showing the main geological features of the Taolin Pb-Zn deposit, modified after Fu et al. (1991)

contact between the Tertiary-Cretaceous sediments and the Neoproterozoic Lengjiaxi Group. The Lengjiaxi Group, a suite of marine, siliciclastic sedimentary rocks with low-grade metamorphism, comprises (carbonaceous) slate, phyllite, schist, quartz sandstone, and quartz phyllite (Xu et al. 2007). The Taolin mining district is characterized by well-developed NE- and nearly E-trending faults that actually define the district-scale Taolin fault zone (Fig. 2a). To the west of the district is the Shitianfan-Qiupingao fault (F_2) which is 19 km long, trends NE, and dips 30–49° to NW. To the south of the district is the Baiyangtian fault (F_1) dipping to SW at angles of 24–64° and together with the F_2 forming a protruding to west, arc-like structural style. This structure has been considered to represent a detachment fault due to the emplacement of the Late Mesozoic (Late Yanshanian) granitoids, resulting in a metamorphic core complex that largely controlled the Taolin Pb-Zn mineralization (Yu et al. 1998; Li and Yu 1991). A voluminous Late Mesozoic granitoids are exposed in the mining district and lithologically are mainly composed of two-mica monzogranites and biotite monzogranites. These granitoids intruded the Lengjiaxi Group and the Cretaceous strata, with the contact surfaces generally dipping to wall rocks at an angle of 30–85°.

The Taolin deposit is mainly hosted within the Shitianfan-Qiupingao detachment fault zone (F_2), and locally occurred in

the Late Mesozoic granitoids and Cretaceous red conglomerates (Fig. 2). This detachment fault zone, with a strike length of about 13 km, mainly consists of orbicular granitic mylonites and tectonic schists with silicification, sericitization, chloritization, and fluoritization. The ore-hosting fault zone consists of seven ore sections from southwest to northeast, namely Shitianfan, Duanshan, Guanshan, Shangtangchong, Yinkongshan, Dujiachong, and Qiupingao. These ore sections seem to have a law of approximately equidistant distribution in space, and along both the strike and inclination the orebodies present expansion, contraction, and pinch-out. Generally, the ore bodies have a strike length up to 2 km and an extension up to 1.2 km along inclination, with the thicknesses varying between 1 and 35 m. The ore occurrence is stable, generally with dipping to NW at an angle of 30–45° (Fig. 2b). The Taolin deposit contains a total metal tonnage of > 0.98 Mt at grades up to 2.35 wt% for Pb+Zn. Among them, the Shangtangchong, Yinkongshan, Guanshan, and Duanshan ore sections are of relatively large sizes and account for 96% reserves of the Taolin mining district.

In general, primary ores are massive, brecciated, and veined (Fig. 3), and are commonly characterized by replacement, crystallization, dissemination, and crosscutting textures (Fig. 4). Sulfide minerals mainly include sphalerite, galena, chalcopyrite, and pyrite (Fig. 4). The gangue minerals are
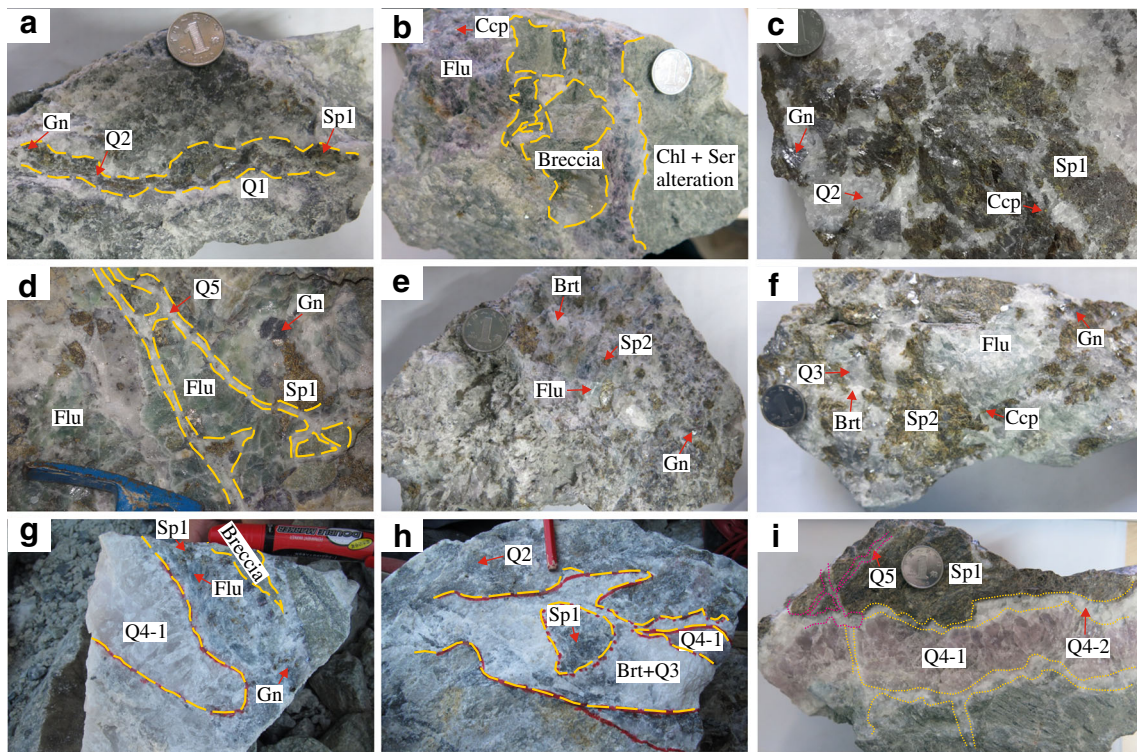
Fig. 3 Photographs showing the occurrences and textures of ores from the Taolin Pb-Zn deposit. **a** Quartz-sulfides vein of the second stage crosscutting the first stage barren quartz. **b** Brecciated-type ores, fluorite with chalcopyritization surrounding the wall rock breccias accompanied by chlorite alteration. **c** Massive-type ores, sulfides coexisted with quartz. **d** Stockwork-type ores, quartz-fluorite-sulfides of the second stage were cut through by the quartz vein of fifth stage. **e** Hand specimen showing quartz, barite, and sulfides. **f** Massive-type ores, hand specimen showing quartz, barite, and sulfides. **g** The fourth stage quartz crosscutting the quartz-fluorite-sulfides vein formed at the second stage, and wall rock breccias occurring in the quartz-fluorite-sulfides vein. **h** Barite with minor sulfide crosscutting quartz-sulfides vein. **i** Late quartz vein crosscut the early minerals. Q, quartz; Sp, sphalerite; Gn, galena; Flu, fluorite; Ccp, chalcopyrite; Brt, barite; Chl, chlorire; Ser, sericite

mainly composed of quartz, fluorite, and barite, with minor chlorite and sericite.

Based on field and microscopic observations and cross-cutting relationships, five hydrothermal mineralization stages, from early to late, were identified (Fig. 5). The first stage is characterized by coarse-grained quartz (Q1) coexisted with minor or no sulfide minerals (Figs. 3a and 4a). The second stage is defined by mineral assemblage of quartz (Q2) + fluorite + sphalerite (Sp1) + galena + chalcopyrite ± pyrite, and defined by Q2 cutting cross Q1 and the Sp1 with claybank color and typically intergrown with galena and fluorite as well as with minor chalcopyrite and pyrite (Figs. 3b–d and 4b–e). In addition, chlorite formed at this stage is closely associated with sulfides (Fig. 4f). The third stage is featured by the mineral assemblage of quartz (Q3) + fluorite + barite + sphalerite (Sp2) + galena + chalcopyrite ± pyrite, with Sp2 present as pale-yellow color and often intergrown with Q3, galena, barite, and fluorite as well as minor pyrite (Figs. 3e–h and 4g–i). Quartz (Q4) formed in the fourth stage of mineralization generally presents as veins crosscutting the earlier minerals and includes two subtypes, i.e., Q4-1 and Q4-2, and coexists with minor

or no sulfide minerals (Figs. 3g–i and 4j). The Q4 mainly occurred in the form of comb texture, with Q4-1 present as light pink color and Q4-2 often formed ringing the Q4-1. With the occurrence of minor sulfides such as chalcopyrite and galena, the fifth stage of mineralization is defined by fine-grained quartz (Q5) which is generally present as vein-lets crosscutting the earlier minerals (Figs. 3d, i and 4k, l).

Hydrothermal alteration primarily include silicification, fluoritization, chlorization, brecciation, and a small amount of sericitization and carbonization (Figs. 3 and 4), of which the silicification, brecciation, chlorization, and fluoritization are intimately related to the Pb-Zn mineralization. Nevertheless, brecciation, as highlighted by abundant breccia which comprises granites, slates, and phyllites, is the main prospecting indicator in the mining district.

Sampling and analytical methods

Ninety-five ore samples were collected from the Taolin deposit in the underground mining pit at the levels ranging from −120 to −180 m. Ten representative samples first
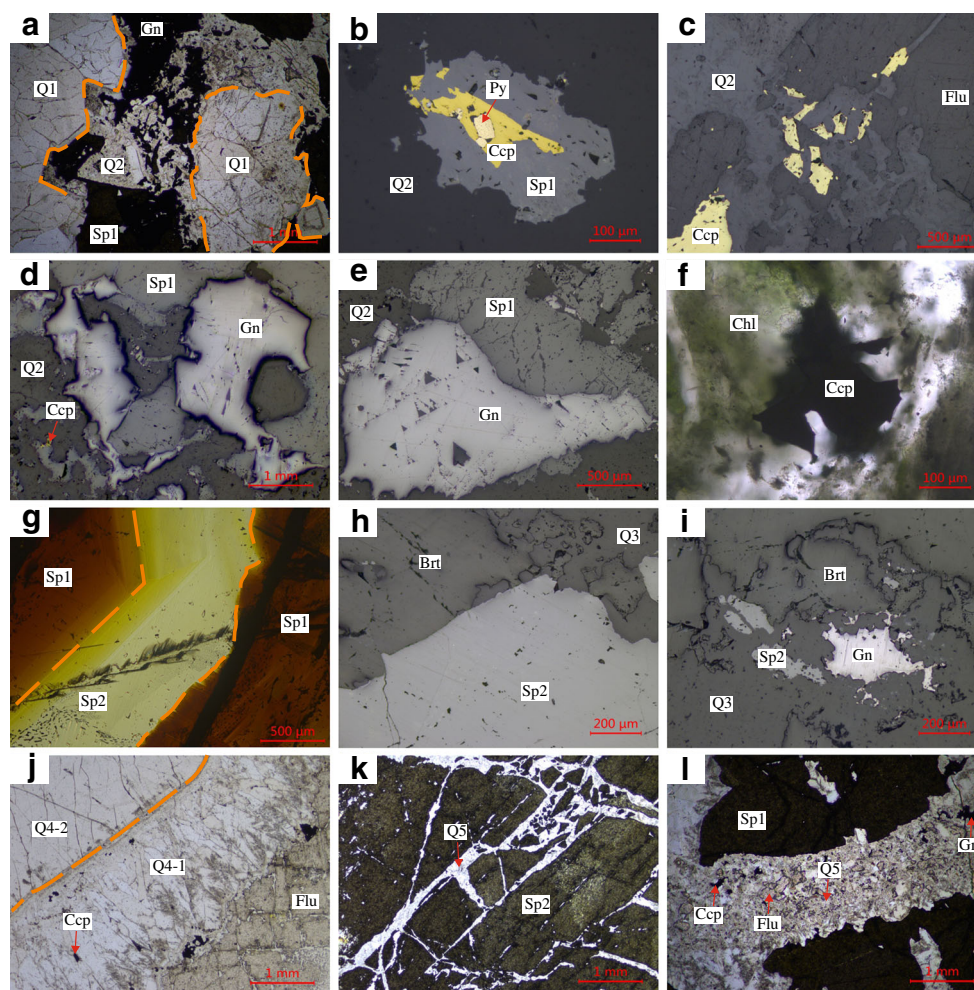
Fig. 4 Photomicrographs showing mineral assemblages and textures of ores from the Taolin Pb-Zn deposit. **a** Coarse-fined quartz (Q1) were crosscut by fine-grained quartz (Q2) associated with sphalerite and galena. Plane-polarized light. **b** Euhedral pyrite and anhedral chalcopyrite grains occurring in sphalerite. Reflected light. **c** Chalcopyrite occurring between the grains of fine-grained quartz (Q2) and fluorite. Reflected light. **d** Sphalerite intergrown with galena, chalcopyrite, and fine-grained quartz (Q2). Reflected light. **e** Fine-grained quartz (Q2) intergrown with sphalerite and galena. Reflected light. **f** Chlorite intergrown with chalcopyrite. Plane-polarized light. **g** The late Sp2 sphalerite veinlet cut cross the early Sp1 sphalerite. Plane-polarized light. **h** Barite intergrown with sphalerite and fine-grained quartz (Q3). Reflected light. **i** Fine-grained quartz (Q3) intergrown with barite, galena, and sphalerite. Reflected light. **j** Comb quartz (Q4-1) and pale pink quartz (Q4-2) crosscut the early minerals. Plane-polarized light. **k** Fine-grained quartz vein (Q5) crosscutting sphalerite. Plane-polarized light. **l** Fine-grained quartz vein (Q5) with minor sulfides crosscutting sphalerite. Plane-polarized light. Q, quartz; Sp, sphalerite; Gn, galena; Py, pyrite; Ccp, chalcopyrite; Flu, fluorite; Brt, barite; Chl, chlorite

were chosen from stages 2 and 3 mineralization for EMPA. The analysis was carried out on sphalerite (Sp1 and Sp2) grains from thin sections. Then the LA-ICP-MS analysis was conducted on the same samples as used for EMPA. Seven samples and five samples from the stages 2 and 3 mineralization were selected respectively for in situ oxygen isotope analysis of quartz by secondary ion mass spectrometry (SIMS) and for in situ sulfur isotope analysis of sulfides and sulfate by laser ablation multi-collector inductively coupled plasma mass spectrometry (LA-MC-ICP-MS). In addition, 7 sulfide separates from the stages 2 and 3 mineralization, and 12 granitoid samples from the Late Mesozoic Mufushan pluton, were analyzed for lead isotope compositions by multi-collector inductively coupled plasma mass spectrometry (MC-ICP-MS).

Electron microprobe analyses

Electron microprobe analyses (EMPA) were performed by JEOL JXA-8230 electron microprobe at the Key Laboratory of Mineralogy and Metallogeny, Guangzhou Institute of Geochemistry, Chinese Academy of Sciences. Polished thin sections of the selected samples were carbon-coated. Operating conditions for spot analyses include an accelerating voltage of 15 kV, an electron beam current of 20 nA, and a beam diameter of 1–2 μm. The following elements were analyzed: Cu, As, Zn, Fe, Ag, Co, Mn, Sn, S, Pb, Cd, Ni. The standard sample, ZnS, was used for S and Zn analysis. Detection limits for analyzed elements are typically less than 300 ppm.

Fig. 5 Mineral paragenesis of the
Taolin Pb-Zn deposit

Fig. 5 Mineral paragenesis of the Taolin Pb-Zn deposit
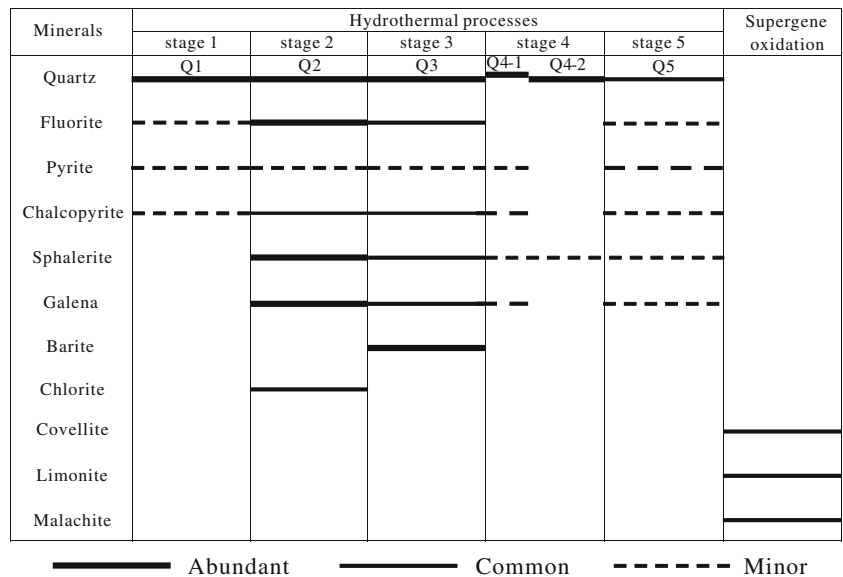
LA-ICP-MS analyses on sphalerite

In situ trace element analyses of the sphalerite (i.e., Sp1, Sp2) were conducted by LA-ICP-MS at Nanjing FocuMS Technology Co. Ltd. The 193-nm ArF excimer laser, homogenized by a set of beam delivery systems, was focused on sulfide surface with a fluence of 3.5 J/cm^2. Ablation protocol employed a spot diameter of 40 μm at a 6-Hz repetition rate for 40 s (equating to 240 pulses). Helium was applied as a carrier gas to efficiently transport aerosol to ICP-MS. The following elements were monitored: ^{49}Ti, ^{51}V, ^{53}Cr, ^{55}Mn, ^{57}Fe, ^{59}Co, ^{60}Ni, ^{65}Cu, ^{66}Zn, ^{69}Ga, ^{72}Ge, ^{75}As, ^{77}Se, ^{93}Nb, ^{95}Mo, ^{107}Ag, ^{111}Cd, ^{115}In, ^{118}Sn, ^{121}Sb, ^{125}Te, ^{182}W, ^{185}Re, ^{197}Au, ^{205}Tl, ^{208}Pb ^{209}Bi, and ^{238}U. USGS polymetallic sulfide pressed pellet MASS-1 and synthetic basaltic glasses GSE-1G were combined for calibration (Gao et al. 2015).

Cathodoluminescence

Cathodoluminescence (CL) imaging of the quartz samples from the stages 2 and 3 mineralization was carried out using a TESCAN MIRA3 field emission scanning electron microprobe (FE-SEM) at the Testing Center, Tuoyan Analytical Technology Co. Ltd. (Guangzhou, China). Working conditions of the CL imaging include 10 kV accelerating voltage and 15 nA beam current.

O-S-Pb isotope geochemistry

The target minerals on thin sections of the stages 2 and 3 ores were cut off, then embedded into epoxy resin, polished, and coated with gold to ensure the sample to be smooth and conductive. Oxygen isotope was analyzed with Cameca
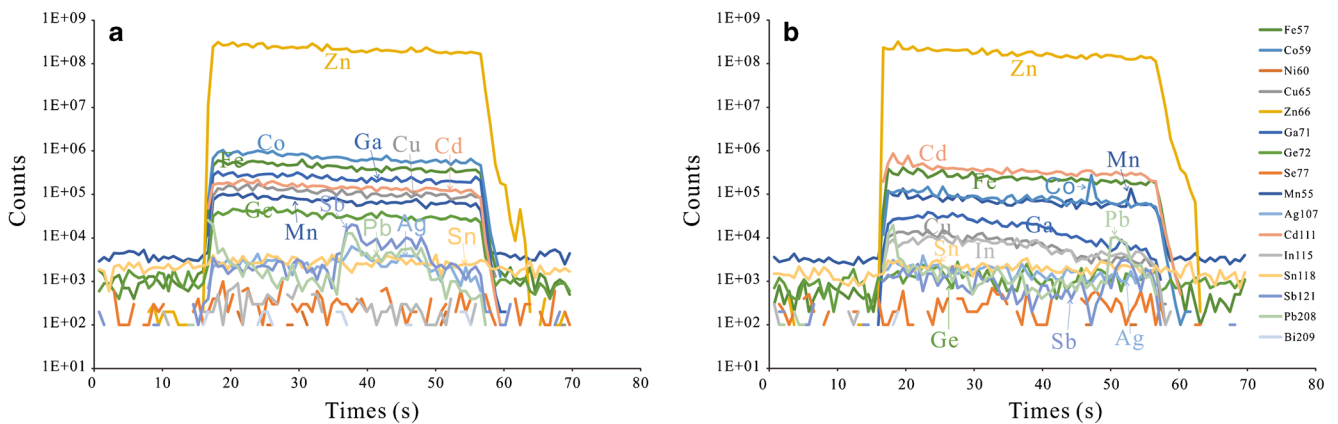

Fig. 6 Representative time-resolved depth profiles for selected elements in sphalerite analyzed in this study. a LA-IC-MS spectra for the Sp1. b LA-IC-MS spectra for the Sp2

IMS1280-HR at the State Key Laboratory of Isotope Geochemistry, Guangzhou Institute of Geochemistry, Chinese Academy of Sciences. Standard NBS28 was used for calibrating the $\delta^{18}O$ values of quartz. Detailed procedures are referred to Yang et al. (2018) for oxygen isotope.

In situ sulfur isotopic analyses of the sulfides and sulfate were carried out using a Nu plasma 1700 multi-collector inductively coupled plasma mass spectrometer (MC-ICP-MS) equipped with a Resolution M-50 193-nm ArF Excimer laser ablation system at the State Key Laboratory of Continental Dynamics, Northwest University. The laser energy density (fluence) used to analyze the S isotope is 3.6 J/cm^2, the frequency is 3 Hz, the spot size is 30 μm, the ablation method is single-point ablation, and the carrier gas is high-purity. The $\delta^{34}S$ can be tested to very high precision (less than 0.1‰). The sulfur isotope ratios of galena, sphalerite, chalcopyrite, and barite were adjusted using the CBI-3 ($\delta^{34}S_{V-CDT} = 28.5 \pm 0.4$‰), NBS123 ($\delta^{34}S_{V-CDT} = 17.8 \pm 0.2$‰), CPY-1 ($\delta^{34}S_{V-CDT} = 4.2 \pm 0.3$‰), and NBS127 ($\delta^{34}S_{V-CDT} = 20.3 \pm 0.2$‰), respectively. For further detailed analytical methods, see Bao et al. (2017), Chen et al. (2017), and Yuan et al. (2018b).

The lead isotopic analyses of seven sulfide separates were performed using a GV Isoprobe-T thermal ionization mass spectrometer monitored by standard NBS 981 at the Analytical Laboratory of the Beijing Research Institute of Uranium Geology, China. Analytical results for the standard NBS981 are $^{206}Pb/^{204}Pb = 16.937 \pm 0.002$ (2σ), $^{207}Pb/^{204}Pb = 15.457 \pm 0.002$ (2σ), and $^{208}Pb/^{204}Pb = 36.611 \pm 0.004$ (2σ). However, whole-rock lead isotopic analyses of 12 granitoid samples were measured by a VG-354 mass spectrometer at the State Key Laboratory of Isotope Geochemistry, Guangzhou Institute of Geochemistry, Chinese Academy of Sciences. About 100 mg powder was weighed into a Teflon beaker, spiked, and dissolved in concentrated HF at 180 °C for 7 h. The lead was separated and purified by a conventional cation-exchange technique (AG1-X8, 20–400 resin) with diluted HBr as an eluant. Repeated analyses of NBS 981 yielded average values of $^{206}Pb/^{204}Pb = 16.933 \pm 0.001$ (2σ), $^{207}Pb/^{204}Pb = 15.486 \pm 0.001$ (2σ), and $^{208}Pb/^{204}Pb = 36.683 \pm 0.002$ (2σ).

Principal component analysis

Principal component analysis (PCA) is a commonly used data analysis method (Belissont et al. 2014; Frenzel et al. 2016; Bauer et al. 2019). PCA transforms the original data into a set of linearly independent representations of each dimension through linear transformation, which can be used to extract the main feature components of the data and for dimensionality reduction of high-dimensional data on the basis of reflecting as much original information as possible (Belissont et al. 2014; Frenzel et al. 2016; Bauer et al. 2019). In addition, since principal component analysis adopts the method of linear dimensionality reduction, the correlation coefficient between each variable and the principal component can be accurately calculated to determine the control variables of the principal component. Therefore, the first two principal components with the highest explained variance (namely, the value of abscissa and ordinate showed in a two-dimensional plane) corresponding to the most significant relationships between the variables. The principal components can also be called contribution rate. Their mathematical meaning is the variance of a principal component as a percentage of the total variance. The higher the contribution rate, the more information that the principal component represents the original variables.

PCA is widely used in the field of geochemical exploration on large-scale datasets to interpret trace element data and to understand their relationship (Winderbaum et al. 2012; Belissont et al. 2014; Frenzel et al. 2016; Wei et al. 2018a; Yuan et al. 2018a; Bauer et al. 2019). PCA has also been found application in isotope geochemistry (Cadoux et al. 2007; Iwamori et al. 2010) and sulfide geochemistry (Winderbaum et al. 2012). Consequently, PCA is applied to the LA-ICP-MS datasets to uncover the pertinence of elements in sphalerite in this study. The database in this study was filtered by the criteria suggested by Yuan et al. (2018a). The important minor and trace elements, such as Fe, Mn, Co, Cu, Ga, Ge, Ag, Cd, In, Sn, and Sb, were selected in this manner. First of all, the values below the detection limit were omitted before processing the dataset. Then, the concentrations of these elements for individual deposit types in a large dataset were log-transformed. Finally, the R software environment was used for data analysis.

Results

EMPA data of sphalerite

EMPA analyses for some trace elements of the stages 2 and 3 sphalerites are listed in ESM 1 Table 1. ESM 1 Table 1 shows that the Sp1 has average values of 62.88 wt% for Zn and 32.55 wt% for S, whereas that the Sp2 has average values of 65.12 wt% for Zn and 32.49 wt% for S. The contents of Fe (averaging 2.12 wt%), Co (averaging 0.04 wt%), and Mn (averaging 0.013 wt%) in Sp1 are higher than those in Sp2 (average values of 0.64 wt% for Fe, 0.01 wt% for Co, and 0.005 wt% for Mn, respectively; ESM 1 Table 1). Cadmium concentrations are approximately equal in both types of sphalerite (0.12 wt% and 0.13 wt% for Cd in Sp1 and Sp2, respectively).

LA-ICP-MS data of sphalerite

The complete LA-ICP-MS dataset composed of 64 spot analyses (ESM 2 Table 2) presents the concentrations of individual

trace elements in sphalerite from the Taolin deposit. The absolute concentration ranges of the selected elements are shown as box-and-whisker plots (Fig. 7) with median and possible outliers of the data. For comparison, the previously published data of sphalerites from Cook et al. (2009), Ye et al. (2011), Wei et al. (2018a, b), and Yuan et al. (2018a) are also presented in Fig. 7.

The elements Mn, Fe, and Co are significantly enriched in Sp1 (63.84–549.9 ppm for Mn, 9809–41373 ppm for Fe, and 162.3–830.1 ppm for Co) relative to those of the Sp2 (12.91–84.09 ppm for Mn, 1190–7626 ppm for Fe, and 39.50–187.6 ppm for Co; ESM 2 Table 2 and Fig. 7a–c), which is consistent with the EMPA results. The Cu, Ga, Cd, and Pb concentrations in both types of sphalerite (Sp1 and Sp2) are similar within the uncertainties (1.937–534.5 ppm Cu, 0.105–628.7 ppm Ga, 425.2–1699 ppm Cd, and 0.070–4.755 ppm Pb for Sp1, and 2.356–677 ppm Cu, 0.436–750.7 ppm Ga, 472.8–1400 ppm Cd, and 0.050–18.30 ppm Pb for Sp2; ESM 2 Table 2 and Fig. 7e–o). The concentrations of In and Sn tend to be slightly higher in Sp1 (0.012–28.35 ppm for In and 0.262–3.549 ppm for Sn) than those in Sp2 (0.029–65.41 ppm for In and 0.270–6.487 ppm for Sn; ESM 2 Table 2 and Fig. 7k, l). In contrast, Sp2 exhibits slightly higher Sb (0.094–33.19 ppm) than Sp1 (0.068–7.606 ppm Sb). The concentrations of Ge, Se, and Ag generally range from 1 to 10 ppm in both types of sphalerite. In addition, concentrations of Ni and Bi in both types of sphalerite are generally less than 1 ppm (ESM 2 Table 2 and Fig. 7d, p). The Ga/In ratios in both the types of sphalerite are much greater than 1 (2.175–3755 for Sp1 and 0.963–7647 for Sp2). Sp1 also displays lower Zn/Fe (16.32–76.83 for Sp1 and 98.64–609.7 for Sp2) and Cd/Fe (0.026–0.118 for Sp1 and 0.067–0.556 for Sp2; ESM 2 Table 2) ratios, when compared with Sp2.

The difference between the concentrations of related trace elements in sphalerite from the Taolin deposit and that from other types is considerable. In contrast to other type deposits (e.g., Skarn, SEDEX, VMS, MVT, and the Jinding type), the Taolin deposit has the highest Co and Ga and the lowest Ag and Cd concentrations (Fig. 7c–j). The elements Mn and Fe are remarkably enriched in Skarn-, SEDEX-, and VMS-type deposits relative to those of the Taolin deposit, but the concentrations of these two elements (Fe and Mn) in the Taolin deposit are slightly higher than those in MVT- and the Jinding-type deposits (Fig. 7a, b). Nevertheless, Cu concentrations in sphalerite from all type deposits are at a high level (generally > 10 ppm). In addition, the sphalerites from MVT- and Jinding-type deposits have conspicuously high concentrations of Ge, Sb, and Pb compared with that of all other types including the Taolin deposit, but the Taolin deposit possesses roughly similar concentrations of Ge, Sb, and Pb to Skarn-, SEDEX-, and VMS-type deposits (Fig. 7g–o). Moreover, the In concentration in the sphalerite from Taolin deposit tend to be slightly higher than those in MVT- and the Jinding-type

deposits, but lower than those in SEDEX- and VMS-type deposits. Tin (Sn) concentrations in SEDEX- and VMS-type deposits are generally higher than those in all other type deposits including the Taolin deposit, whereas Se concentrations with a large variation in Skarn-type deposits are higher than those in all other type deposits (Fig. 7h, l).

Quartz textures

CL imaging was used in the Taolin deposit to reveal the hydrothermal quartz textures of the stages 2 and 3 mineralization. Quartz grains from the stage 2 (Q2) mineralization commonly possess relatively homogeneous dark luminescence without obvious bands or zonation (Fig. 8a). However, quartz grains from the stage 3 (Q3) generally show obvious euhedral-subhedral core-rim texture, characterized by light to dark color zones from core to rim (Fig. 8b). Contact among these two zones lacks any replacement texture, suggesting that they are growth zones. The light core is relatively wide and lacks clear oscillatory zoning, whereas the dark rim is narrow and has slight oscillatory zoning.

O-S-Pb isotopic components

The in situ oxygen isotopes of quartz from the Taolin deposit are plotted in Fig. 12 and listed in ESM 3 Table 3. The $\delta^{18}O$ values of the stage 2 quartz (Q2) are relatively high but narrowly span from 14.3 to 17.9‰ (Fig. 12 and ESM 3 Table 3), whereas that of the stage 3 quartz (Q3) range from 9.7 to 14.4‰ (Fig. 12 and ESM 3 Table 3).

Thirty-nine in situ analyses on sulfur isotopes of sphalerite, galena, chalcopyrite, and barite from the Taolin deposit are listed in ESM 4 Table 4 and presented in Fig. 13. The $\delta^{34}S_{VCDT}$ values of sulfides from the stage 2 ores range from − 8.8 to − 1.9‰, with the $\delta^{34}S_{VCDT}$ values of sphalerite from − 2.6 to − 1.9‰, chalcopyrite from − 4.7 to − 3.8‰, and galena from − 8.8 to − 5.1‰. The $\delta^{34}S_{VCDT}$ values of sulfides and sulfate from the stage 3 ores range from 12.6 to 17.7‰ for barite, from − 4.2 to − 3.4‰ for sphalerite, and from − 8.2 to − 6.7‰ for galena.

The analytical results on lead isotopes of three sphalerite and four galena separates from the Taolin deposit are displayed in Fig. 14 and ESM 5 Table 5. As a whole, the isotopic ratios of sulfides from Taolin fall in a small range, with $^{206}Pb/^{204}Pb$ ranging from 18.130 to 18.226 (average 18.174), $^{207}Pb/^{204}Pb$ from 15.629 to 15.752 (average 15.684), and $^{208}Pb/^{204}Pb$ from 38.619 to 39.000 (average 38.791). The whole-rock lead isotopic compositions for the 12 Mufushan granitoid samples are also listed in ESM 5 Table 5. The $^{206}Pb/^{204}Pb$, $^{207}Pb/^{204}Pb$, and $^{208}Pb/^{204}Pb$ ratios for whole-rock lead isotopic compositions of the granitoids vary from 18.039 to 18.323 (average 18.190), from 15.650 to 15.674 (average 15.661), and from 38.362 to 38.755 (average 38.550), respectively. All these lead isotope data plot
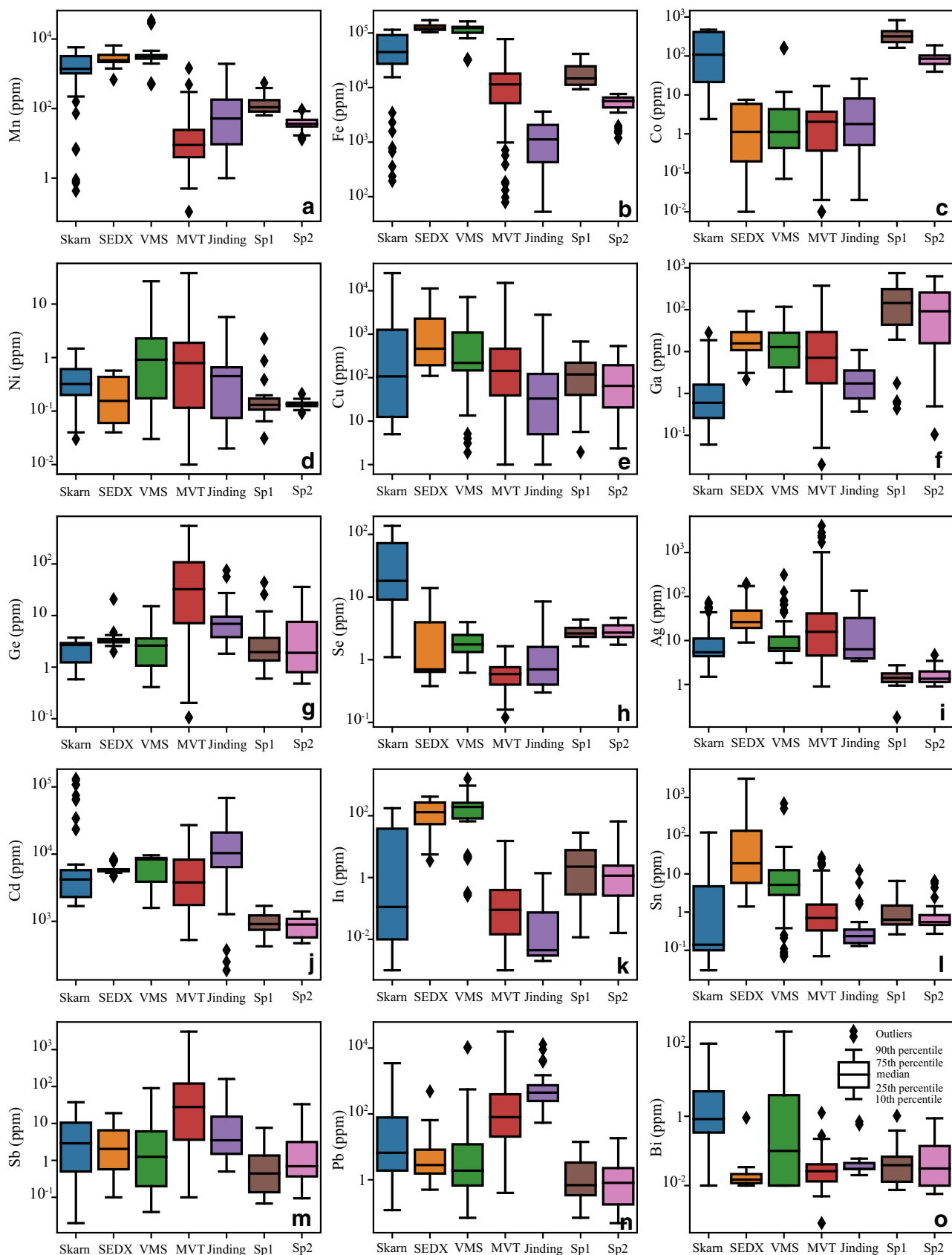
Fig. 7 Trace element contents (LA-ICP-MS) in sphalerite from the Taolin deposit and those collected in Cook et al. (2009), Ye et al. (2011), Wei et al. (2018a, 2018b), and Yuan et al. (2018a) varying by Skarn, SEDX, VMS, MVT, and special Jinding

Fig. 8 CL images of quartz from the Taolin deposit. **a** Homogeneous CL of Q2, without growth bands or zoning. **b** Core-rim texture of Q3. Abbreviations as in Fig. 4
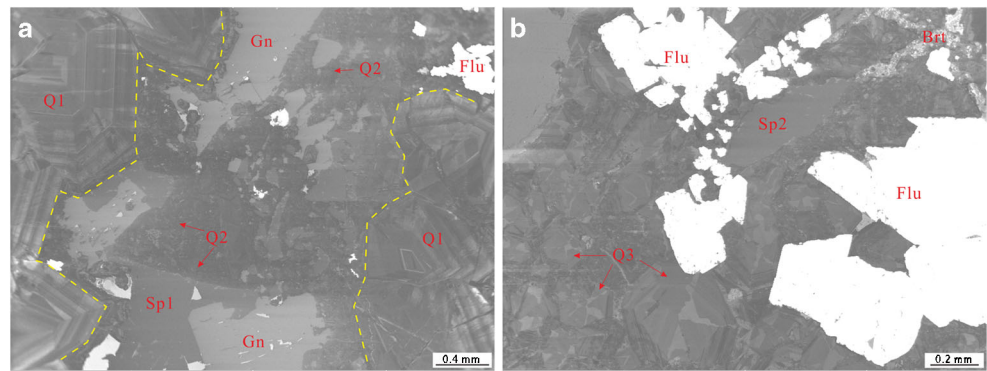
above the Orogen line on the $^{207}Pb/^{204}Pb$ vs. $^{206}Pb/^{204}Pb$ diagram (Fig. 14) and show a relatively clear liner array approximately parallel to the orogen, mantle, and upper crust curves on the $^{208}Pb/^{204}Pb$ vs. $^{206}Pb/^{204}Pb$ diagram (Fig. 14).

Principal component analysis of minor and trace elements

The results of the PCA are shown in Fig. 10. The first two principal components (PC1 and PC2) account for 60.6% of the total variance. Element distributions (Fig. 10b) highlight three groups. The first group consists of Cu, Ga, Ge, Sn, In, and Ag (loading PC1), while the second group is composed of Mn, Fe, Co, and Cd (loading PC2). The third group is composed of Sb (loading PC3). All of them have positive signs and are positively correlated (Fig. 10b). Thereinto, PC1 can be divided into PC1-1 (Cu, Ga, Ge, Ag) and PC1-2 (Sn, In) two subgroups; PC2 also can be divided into two subgroups: PC2-1 (Mn, Fe, Co) and PC2-2 (Cd). Elements showing similar behavior are highlighted in three clusters in the PC1 vs. PC2 plane (Fig. 10b). PC2-1 (loaded by Mn, Fe, Co) is correlated with the spots in claybank Sp1. Spots analyses in the pale-yellow Sp2 exhibit a relatively well-marked anti-correlation with PC2-1.

Discussion

Substitution of minor and trace elements in sphalerite

Time-resolved depth profiles usually exhibit ragged or spiky patterns when microscopic inclusions are hosted in sphalerite (Cook et al. 2009; Ye et al. 2011). On the contrary, these profiles are generally flat when elements are present as solid solution. According to Fig. 6 a, b, it is suggested that Fe, Cd, Co, and Mn occur as solid solution, whereas Ag, Cu, Pb, Ni, Ga, Ge, Se, Bi, Sb, In, and Sn occur as mineral inclusions or solid solution.

Many workers have undertaken laboratory experiments on the substitution mechanisms in sphalerite (e.g., Cook et al. 2009; Belissont et al. 2014; Frenzel et al. 2016; George et al.

2016; Yuan et al. 2018a; Bauer et al. 2019; Zhuang et al. 2019). For example, Zn^{2+} being replaced by Fe^{2+}, Cd^{2+}, Mn^{2+}, Co^{2+}, Ni^{2+}, Hg^{2+}, and Sn^{2+}, such these simple substitutions have been discovered by Seifert and Sandmann (2006) and Murakami and Ishihara (2013). Besides, there are more complicated substitution mechanisms also occur in sphalerite (Belissont et al. 2014; Frenzel et al. 2016; George et al. 2016; Yuan et al. 2018a). A binary diagram of trace element contents in sphalerite could reveal distinct positive or negative correlations between certain elements, which can provide some information and discriminate the different substitution mechanisms.

In this study, the concentrations of Fe, Mn, and Co in Sp1 or Sp2 display a distinct positive correlation (Fig. 9f, h). Besides, the Fe and Cd are positively correlated although the correlation is not conspicuous (Fig. 9g). Thus, the direct substitutions ($Zn^{2+} \leftrightarrow Fe^{2+}$, $Zn^{2+} \leftrightarrow Mn^{2+}$, $Zn^{2+} \leftrightarrow Co^{2+}$, $Zn^{2+} \leftrightarrow Cd^{2+}$) mentioned above were verified (Seifert and Sandmann 2006; Murakami and Ishihara 2013).

Germanium usually occurs as Ge^{4+} in sphalerite, although its divalent cation Ge^{2+} appears occasionally (Ye et al. 2011). Some correlations between Ge and other monovalent cations (i.e., Cu^+ and Ag^+) were found in sphalerite from the Taolin deposit. Trace element contents of Cu and Ge exhibit a positive correlation that is parallel to the line of $(Cu/Ge)_{mol} = 2$ (Fig. 9a). Therefore, the possible substitution mechanism is $3Zn^{2+} \leftrightarrow 2Cu^+ + Ge^{4+}$. In addition, another positive correlation between Ag and Ge, with a trend that is subparallel to the line of $(Ag/Ge)_{mol} = 2$ (Fig. 9b), raises the potential substitution of $3Zn^{2+} \leftrightarrow 2Ag^+ + Ge^{4+}$.

A general substitution mechanism would lead to the enrichment of mono-, tri-, and tetravalent cations (i.e., Ag^+, Cu^+, Sb^{3+}, Ga^{3+}, In^{3+}, Ge^{4+}, and Sn^{4+}) (Cook et al. 2009). As shown in Fig. 10 b, these elements show a strong correlation highlighted by PCA. Figure 9c further confirms the strong linear correlation among these elements. When it comes to concentration, Cu is the predominant monovalent cation and Cu (and Ag to a lesser extent) concentration is close to the sum of tri- and tetravalent cations (Fig. 9c). Consequently, Cu could be responsible for the incorporation of these trivalent/tetravalent cations.
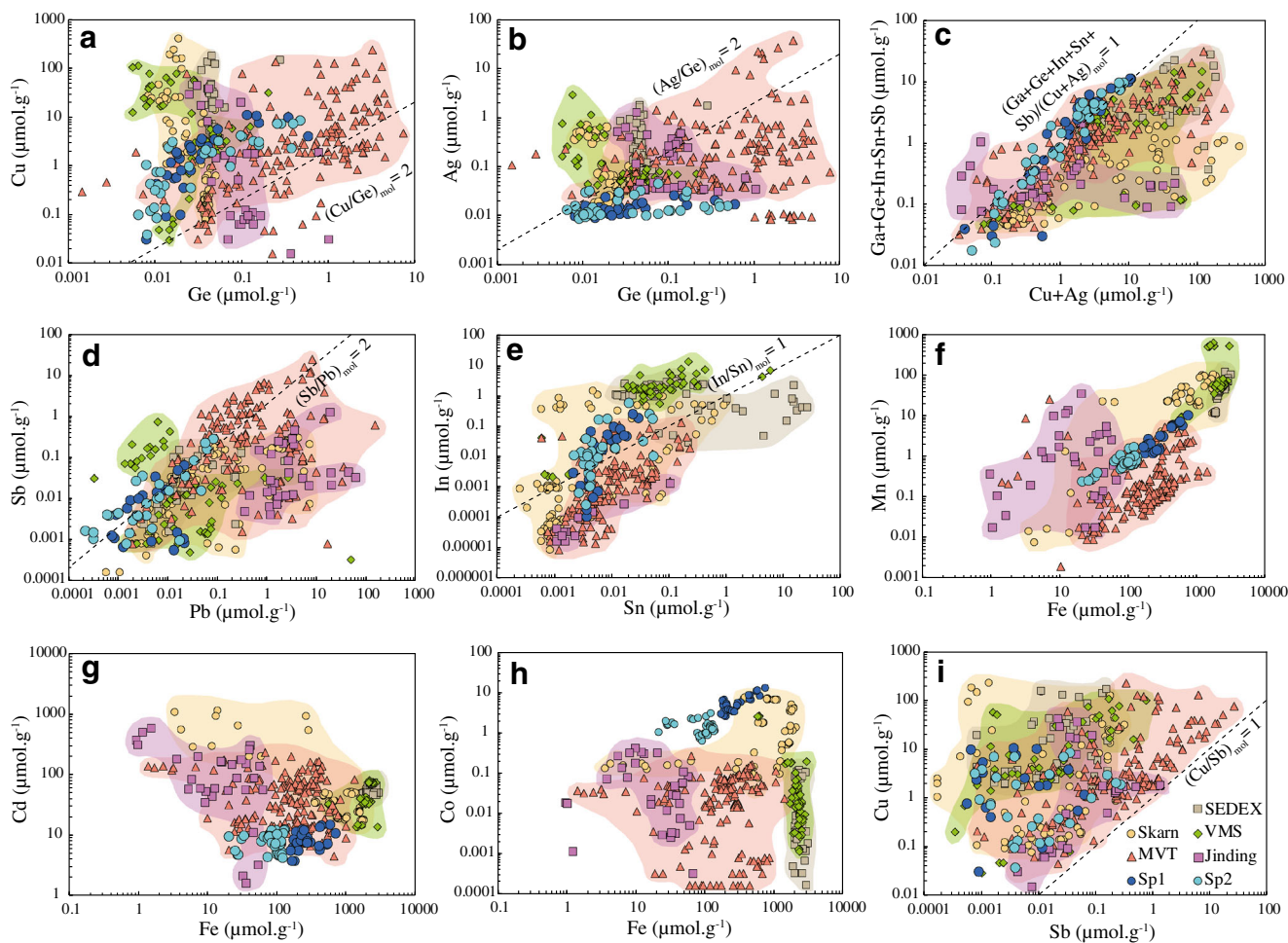
Fig. 9 Correlation plots of **a** Cu vs. Ge, **b** Ag vs. Ge, **c** (Ga+Ge+In+Sn+Sb) vs. (Cu+Ag), **d** Sb vs. Pb, **e** In vs. Sn, **f** Mn vs. Fe, **g** Cd vs. Fe, **h** Co vs. Fe, and **i** Cu vs. Sb. Note that the dashed lines represent the theoretical mole ratios implying the potential substitution mechanisms of trace elements trapped in sphalerite crystal

Although the concentrations of Sb and Pb are at a low level, the positive correlation that is parallel to the line of $(Sb/Pb)_{mol} = 2$ (Fig. 9d) between them suggests a reasonable coupled substitution $4Zn^{2+} \leftrightarrow 2Sb^{3+} + Pb^{2+} + \square$ (vacancy).

Tin generally exhibits Sn^{2+}, Sn^{3+}, and Sn^{4+} oxidation states; however, its mechanism of incorporation remains controversial. The weak positive trend between In and Sn, with a slope of 1 (Fig. 9e), thus indicates that the existence of the three possible substitutions ($3Zn^{2+} \leftrightarrow In^{3+} + Sn^{3+} + \square$, $3Zn^{2+} \leftrightarrow In^{3+} + Sn^{2+} + (Cu, Ag)^+$, and $4Zn^{2+} \leftrightarrow In^{3+} + Sn^{4+} + (Cu, Ag)^+ + \square$).

The contents of Cu and Sb display a positive correlation that is parallel to the line of $(Cu/Sb)_{mol} = 1$ (Fig. 9i), suggesting a possible substitution mechanism of $2Zn^{2+} \leftrightarrow Cu^+ + Sb^{3+}$.

Physicochemical conditions of mineralization

The concentrations of some elements in sphalerite are largely influenced by ore-forming temperature (Gao et al. 2016). Previous studies (Liu et al. 1984; Cook et al. 2009; Ye et al. 2011, 2012; Zou et al. 2012) have shown that the sphalerite formed under high temperature is dark in color and enriched in Fe, Mn, In, and Se, along with the Ga/In ratio usually less than 0.1. In contrast, the sphalerite formed under moderate temperature condition is enriched in Cd and In, with the Ga/In ratio generally between 0.1 and 5.0 (Liu et al. 1984; Gao et al. 2016). Besides, under low temperature, the sphalerite has a relatively high concentration of Ga, Ge, and Ag, with light color and Ga/In ratio > 1 (Liu et al. 1984; Gao et al. 2016). The concentrations of Fe and Mn in sphalerite from the Taolin deposit are consistent with that in MVT Pb-Zn deposit; however, In and Se concentrations are higher in comparison to those from MVT Pb-Zn deposit as mentioned above. Furthermore, the sphalerite from Taolin deposit is rich in Ga, with Ga/In ratios ranging from 0.96 to 7647 (generally > 10; see ESM 2 Table 2), indicating that the Taolin sphalerite might be formed under medium-low temperature conditions. Besides, the Fe content in sphalerite often has a positive correlation with mineralization temperature (Liu et al. 2010), with
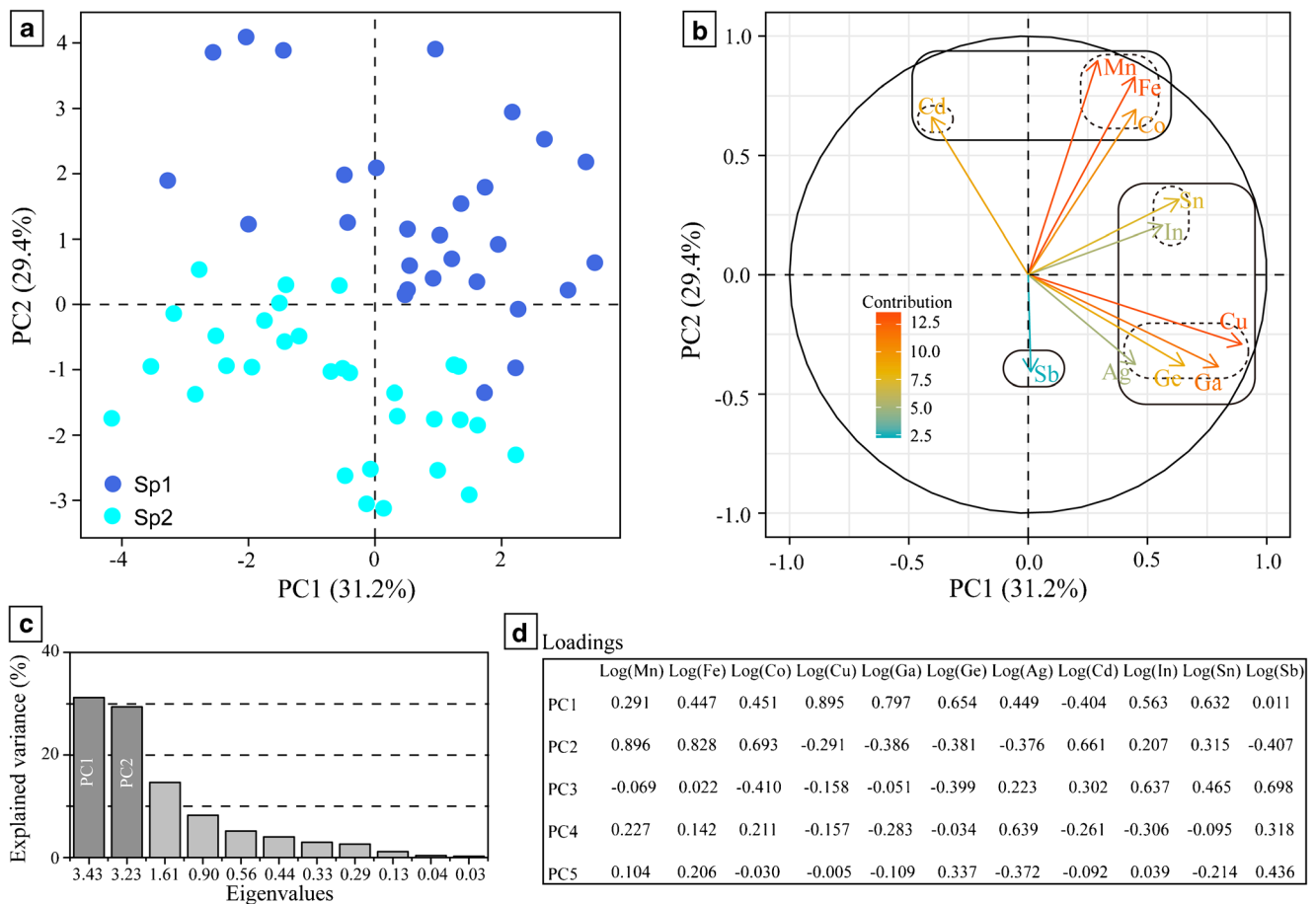
Fig. 10 PCA of the log-transformed LA-ICP-MS dataset of trace element compositions in sphalerite from Taolin deposit. **a** Score plot of all data points, and corresponding histograms of PC1 and PC2 for the trace element composition of the two stages of sphalerite. **b** Loading plot of the

PCA showing the elements (i.e., variables) and framed groups of elements with similar behavior. **c** Scree plot of the eigenvalues of the correlation matrix, explaining the variance. **d** Loadings of the principal components

Zn/Fe ratios usually < 10, 10–100, and > 100 for sphalerite formed at medium-high (250–300 °C), medium (150–250 °C), and low (< 150 °C) temperatures, respectively (Yu et al. 1987). The Zn/Fe ratios of the Taolin sphalerite range from 16.32 to 76.83 (av. 50.15) for Sp1 and from 98.64 to 609.7 (av. 191.6) for Sp2, indicating a medium temperature for Sp1 formation and lower temperature for Sp2 generation. The sphalerite geothermometer (GGIMFis) proposed by Frenzel et al. (2016) was used to calculate ore-forming temperatures and calculated temperatures are 206 ± 43 °C for Sp1 and 169 ± 37 °C for Sp2, similar to that on the basis of Zn/Fe ratio (ESM 2 Table 2). These estimated temperatures are consistent with the corresponding fluid inclusion data, which yield homogenization temperatures of 120–200 °C (Roedder and Howard 1988). Consequently, the Taolin Pb-Zn deposit most likely formed under medium-low temperature conditions.

The concentration of Fe in sphalerite is largely affected by temperature and sulfur fugacity (Scott and Barnes 1971; Hutchison and Scott 1983; Kelly et al. 2004; Keith et al.

2014). The lower values (av. 1.14%) of FeS mol% for the Sp2 than that (av. 3.73%) for the Sp1 (ESM 1 Table 1) suggest that from the stage 2 to stage 3 of mineralization at Taolin, the sulfur fugacity increased, whereas that the ore-forming temperatures decreased as suggested above.

Because Mn enters the crystal lattice of sphalerite in the form of MnS (Bernardini et al. 2004; Kelly et al. 2004), the concentrations of Mn in sphalerite are strongly influenced by redox conditions. The Mn concentration in sphalerite generally has a positive correlation with reduction degree (Kelly et al. 2004). Therefore, at Taolin, a higher Mn content for Sp1 than that for Sp2 indicates a relatively more reduced environment for the early stage (i.e., the stage 2) of mineralization.

Sources of ore-forming fluids

Oxygen isotope is a common and effective way to trace the possible origin of ore-forming fluids (Jiao et al. 2017). The $\delta^{18}O$ value of the hydrothermal fluid can be calculated via the
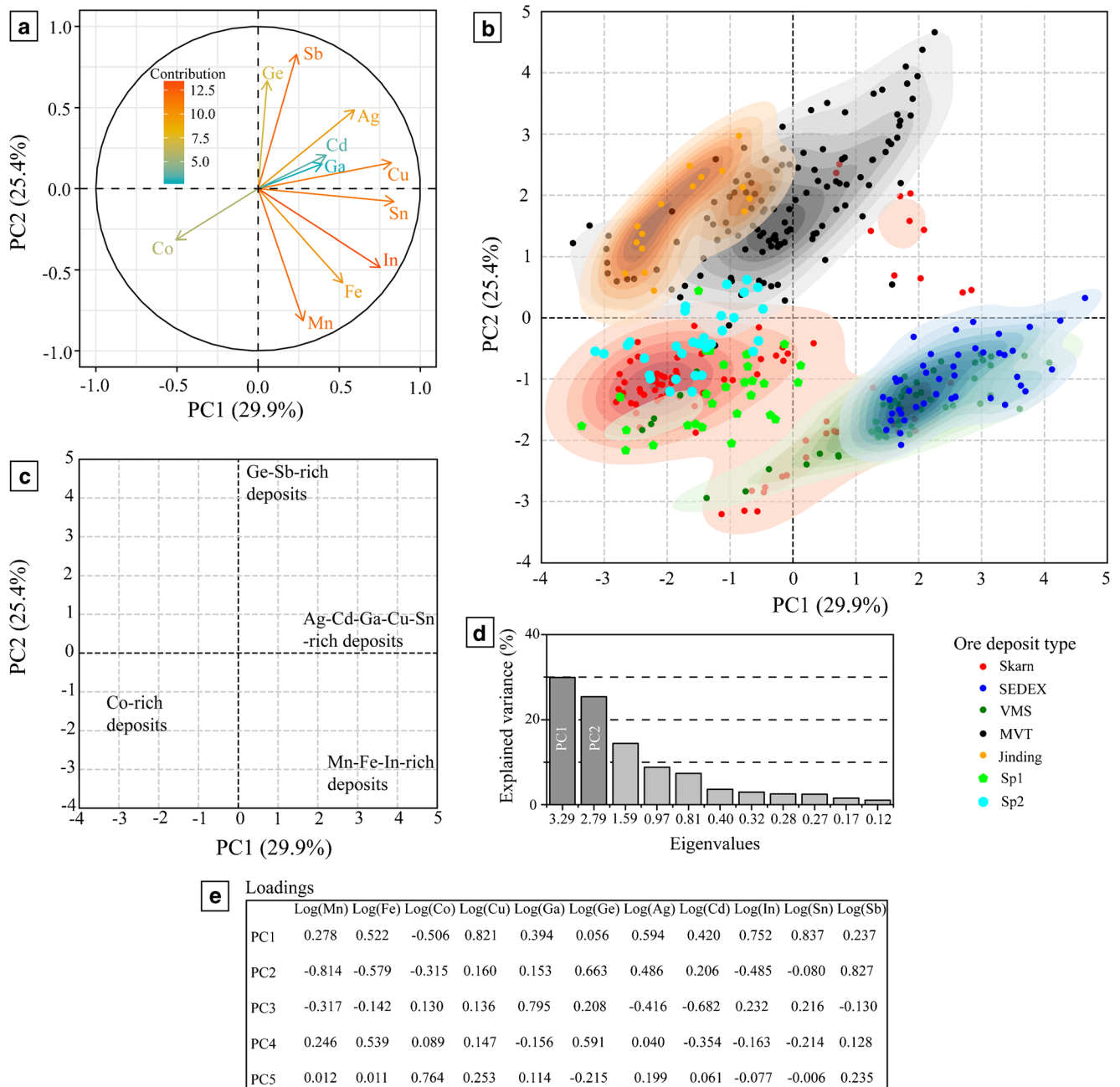
Fig. 11 PCA of Taolin deposit and Cook et al. (2009), Ye et al. (2011), Wei et al. (2018a, 2018b), and Yuan et al. (2018a) LA-ICP-MS dataset of sphalerite of different ore deposits from various types worldwide. Eigenvalues and loadings of the PCA are indicated. **a** Plot of the elements (variables). **b** The scatter plot of the log-transformed spot analysis datasets (individuals) of the above publications including the Taolin dataset, plotted in the PC1 vs. PC2 plane. **c** Interpretative scheme in terms of element enrichment for spot analysis (individuals). **d** Scree plot of the eigenvalues of the correlation matrix, explaining the variance and scores legend (i.e., ore deposit types). **e** Loadings (i.e., extracted eigenvectors) of the principal components

equation: $1000 \times \ln\alpha_{quartz\text{-}H2O} = 4.28 \times 10^6 \times T^{-2} - 3.5 \times 10^3 \times T$ (Sharp et al. 2016). The oxygen isotopic features of the ore-forming fluids for the stages 2 and 3 of mineralization, recalculated using the temperatures constrained by sphalerite geothermometer of Frenzel et al. (2016) (GGIMFis), are presented in Fig. 12. The samples from the stage 2 show relatively high $\delta^{18}O_{fluid}$ (− 0.2 to 8.9‰) values (Fig. 12 and ESM 3

Table 3), which cover most values of magmatic water (5.5–10‰; Taylor 1974). Besides, the Cd/Fe ratio of sphalerite can provide important information about whether or not magmatism was involved in the ore-forming process(es), because the Cd/Fe ratio of sphalerite associated with magmatism is usually < 0.1 (Zhao et al. 2007; Cao et al. 2014). In this study, the average Cd/Fe ratio of 0.1 for the Sp1 from the

Fig. 12 $\delta^{18}O_{quartz}$ and $\delta^{18}O_{fluid}$ values for Taolin deposit. $\delta^{18}O$ of magmatic-derived fluid is higher than $\delta^{18}O_{fluid}$ of Taolin quartz samples, which indicates the magmatic fluid is balanced by meteoric water during ore formation; the area of magmatic water is from Taylor (1974)
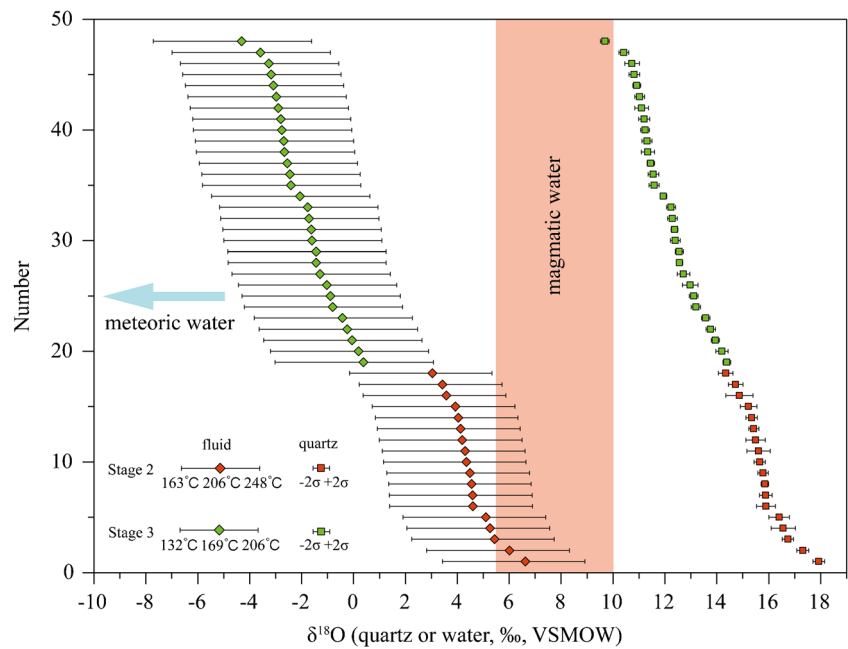
Taolin deposit (ESM 2 Table 2) reveal that the early mineralization most likely had a genetic link to magma-related hydrothermalism. The $\delta^{18}O_{fluid}$ (− 7.7 to 3.1‰) values of the stage 3 fluids are relatively depleted, and strongly indicate the involvement of an isotopically lighter component, such as meteoric water. Therefore, the ore-forming fluids in the Taolin deposit are dominant of magmatic water origin at the stage 2 of mineralization due to the emplacement of the Late Mesozoic Mufushan granitic pluton, and then most likely were mixed with meteoric water at the stage 3 of mineralization.

Constraints on the ore-forming materials

In general, the sulfur isotopic composition of sulfides could not represent the sulfur content ($\delta^{34}S_{\Sigma S}$) of the ore fluids, which is influenced by oxygen fugacity (f_{O2}), temperature, pH, and ionic strength (Ohmoto 1972). Hence, the S sources in the Taolin deposit must be determined based on the total S isotopic signature of the hydrothermal fluids when the sulfides were deposited. However, when the hydrothermal fluids are dominated by H_2S with low oxygen fugacity and low pH values, the relationship $\delta^{34}S_{\Sigma} \approx \delta^{34}S_{H2S} \approx \delta^{34}S_{pyrite}$ holds in the equilibrium state (Wu et al. 2014). The sulfides from the stage 2 of the Taolin Pb-Zn mineralization are dominated by sphalerite, galena, and chalcopyrite, where no sulfate minerals have been detected. Therefore, H_2S is predominant in the hydrothermal system at stage 2, and sphalerite, galena, and chalcopyrite formed in the environment with low f_{O2} and low pH values. According to ESM 4 Table 4, the basic sequence ($\delta^{34}S_{Sp} > \delta^{34}S_{Ccp} > \delta^{34}S_{Gn}$) of sulfides from the Taolin deposit is consistent with the $\delta^{34}S$ enrichment condition of

$\delta^{34}S_{Sp} > \delta^{34}S_{Ccp} > \delta^{34}S_{Gn}$ at isotopic equilibrium, indicating that the S isotopes of sphalerite, galena, and chalcopyrite had reached equilibrium (Ohmoto 1986). Consequently, $\delta^{34}S_{H2S}$ values of sphalerite, galena, and chalcopyrite can represent the total S isotopic compositions of the hydrothermal system (Xu et al. 1993). The $\delta^{34}S_{H2S}$ values were calculated with the equation $\delta^{34}S_{H2S} = \delta^{34}S_i - A_i (10^6 \times T^{-2})$, where i stands for different sulfides; A_i value is 0.1 for sphalerite, 0.05 for chalcopyrite, and − 0.64 for galena, respectively; T is the temperature in Kelvin (Li and Liu 2006); and the average of sphalerite geothermometry from Frenzel et al. (2016) was used to calculate the $\delta^{34}S_{H2S}$ value. The $\delta^{34}S_{H2S}$ values of the stage 2 sulfides vary from − 3.1 to − 2.3‰ for sphalerite, − 4.9 to − 4.0‰ for chalcopyrite, and − 6.0 to − 2.4‰ for galena (Fig. 13a and ESM 4 Table 4). These $\delta^{34}S$ values are consistent with that of most igneous rocks within a range of 0 ± 5‰ (Ohmoto and Rye 1979), indicating that the sulfur for the stage 2 mineralization was mainly derived from a magmatic source.

In addition to sulfides, barite was also discovered in the stage 3 of mineralization (Fig. 4h, i). Sphalerite and galena from this stage display distinctly lower $\delta^{34}S$ values than that of barite (ESM 4 Table 4). Because sulfur isotopes can be redistributed between oxidized and reduced species during precipitation (Gomide et al. 2013), the actual $\delta^{34}S$ ($\delta^{34}S_{\Sigma S}$) of the hydrothermal liquids cannot be represented by the mean $\delta^{34}S$ values of either sulfides or sulfates in this case. The $\delta^{34}S_{\Sigma S}$ of the hydrothermal liquids has been calculated using sphalerite, galena, and co-genetic barite as mineral pairs and using the δ-δ diagram (Fifarek and Rye 2005) (Fig. 13b). As estimated from the intersection of a straight line fit to the data with the line of unit slope which shows no sulfide-sulfate fractionation

Fig. 13 **a** Histogram of δ^{34}S values of fluids of stage 2. **b** Plots of δ^{34}S$_{galena}$, δ^{34}S$_{sphalerite}$ vs. δ^{34}S$_{barite}$ values for sulfide and sulfate mineral assemblages from stage 3, the straight line of negative slope represents a co-variation in δ^{34}S$_{sulfide}$ and δ^{34}S$_{sulfate}$ values generated through SO$_4^{2-}$-H$_2$S isotope exchange over a wide range of temperatures (Fifarek and Rye 2005), the absolute value (0.33, 0.27) of the slope of the straight line is equivalent to the molar ratio of SO$_4$/H$_2$S in the liquids, the δ^{34}S$_{\Sigma S}$ value of the hydrothermal liquids range between − 2.3 and − 0.3‰, estimated from the inter-section of the straight line with the line of unit slope which is char-acterized by non sulfide-sulfate fractionation (Δ = 0‰). Abbreviations as in Fig. 4
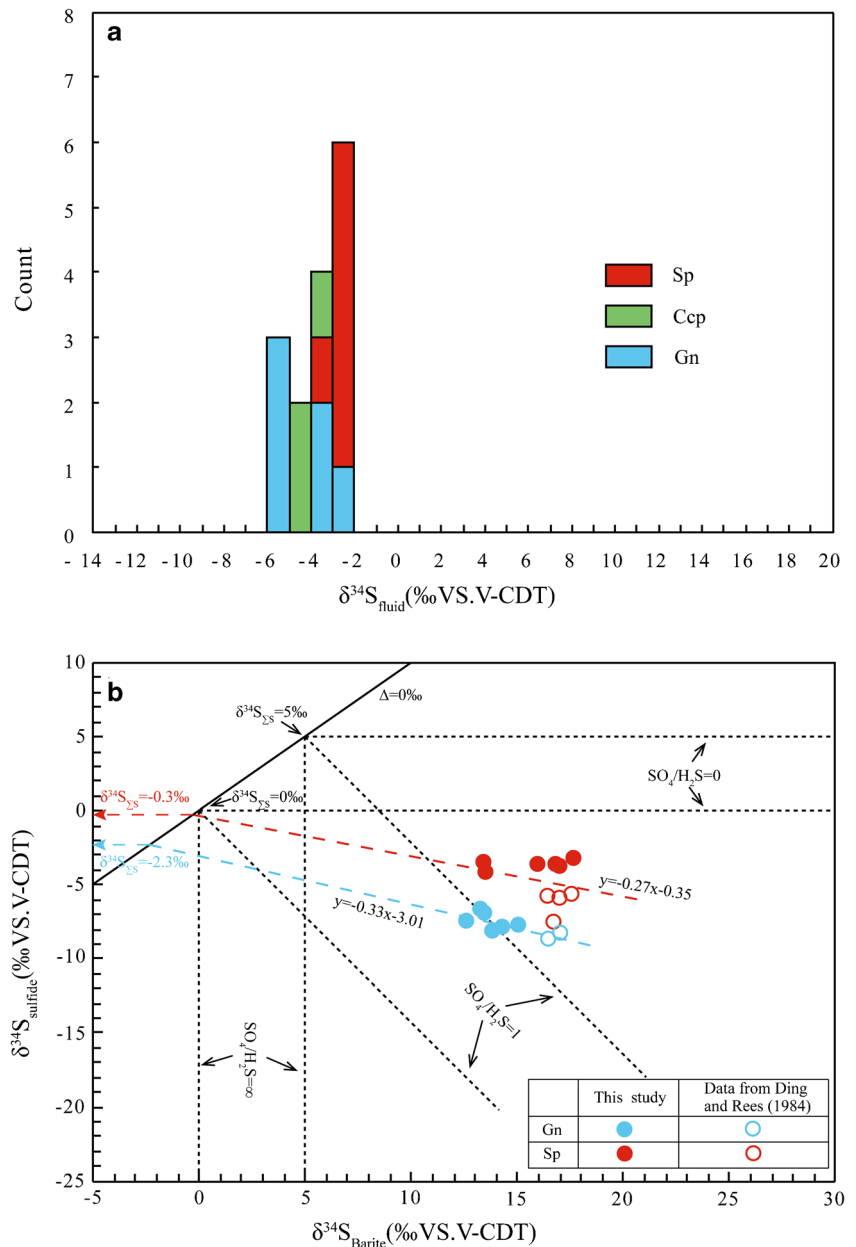

(Δ = 0‰), the δ^{34}S$_{\Sigma S}$ value of the precipitating liquids is es-timated to be around − 2.3‰ for galena-barite mineral pair and − 0.3‰ for sphalerite-barite mineral pair, suggesting a predominant magmatic sulfur origin. The upward trend of δ^{34}S$_{\Sigma S}$ of the ore fluids from the stages 2 to 3 of mineraliza-tion at Taolin most likely was caused by the precipitation of sulfides with negative δ^{34}S values at stage 2, as suggested by Ding and Rees (1984). Based on the corrected sulfur isotopes, the ore-forming fluid for the stage 3 mineralization most likely originated from the same source(s) as that for the stage 2, i.e., both from magmatic water.

For comparison, lead isotopic data of the ten galena and two plagioclase separates from Ding et al. (1986) is also presented in Fig. 14 and ESM 5 Table 5. In Fig. 14 a,

most of the analyzed samples are plotted near to or above the upper crust curve, with the remainders in the fields between the upper crust and the mantle curves. Furthermore, all the Taolin ores, Mufushan granitoids, and Lengjiaxi Group rocks have more radiogenic Pb than that of the mantle and the lower crust (Fig. 14a), revealing the possible source(s) of lead from the upper crust for the Taolin Pb and Zn mineralization. The diagram of ^{208}Pb/^{204}Pb vs. ^{206}Pb/^{204}Pb (Fig. 14b) further reflects that the analyzed samples have a clear liner array approxi-mately parallel to the orogen, mantle, and upper crust curves. The Pb isotopic components of sulfides in the ores from the Taolin deposit are similar to those of the Mufushan pluton mainly composed of two-mica

Fig. 14 Plots of lead isotopic compositions of the Taolin deposit. Reference lines are based on Zartman and Doe (1981). Data of the sulfides, plagioclase, and Mufushan granitoids are from this study and Ding et al. (1986), the Neoproterozoic Lengjiaxi Group from Liu and Zhu (1994)
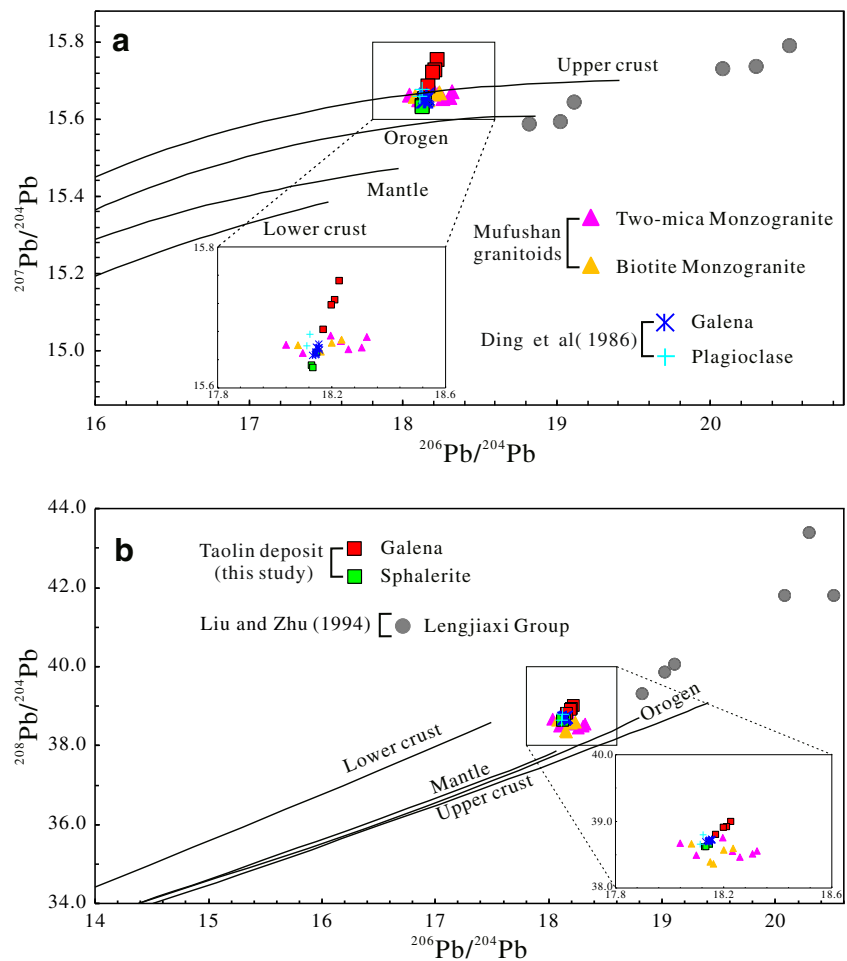
monzogranite and biotite monzogranite, but are significantly different from those of the Lengjiaxi Group rocks (Fig. 14 and ESM 5 Table 5). This suggests that the ore metals (Pb and Zn) may have been derived from the Mufushan pluton rather than the Lengjiaxi Group rocks.

Type and implications for Pb-Zn mineralization

Previous studies have shown that the concentrations of trace elements in sphalerite from different types of Pb-Zn deposits are variable (Cook et al. 2009; Ye et al. 2011; Belissont et al. 2014; Frenzel et al. 2016; Yuan et al. 2018a). Considering these different geochemical signatures in certain elements, the possible genesis can be obtained according to Fig. 9 as mentioned above. For example, sphalerite from magmatism-related deposits (i.e., SEDEX and VMS deposits) shows enrichment in In, Sn, Fe, and Mn. Those from magmatism-related deposits (i.e., skarn deposits) are enriched in Fe, Mn, and Co. In contrast, sphalerites from deposits unrelated to a magmatic source (i.e., MVT deposits and Jinding deposit) are characterized by high Ge, Ag, Sb, Cd, and Pb contents. The Taolin deposit shows high concentrations of Co in sphalerite,

which is consistent with the sphalerite from magmatism-related deposits (i.e., skarn deposits).

According to the Fig. 11, the results of PCA show that the first factor PC1 is mainly loaded with Ag, Cu, Sn, In, and Co, the second-order PC2 is primarily loaded with Ge, Sb, Mn, and Fe, and that the third factor PC3 is loaded with Cd and Ga (Fig. 11a). Thereinto, the first two factors account for 65.3% of element content variability. Three element clusters, i.e., (Ge, Sb), (Ag, Cu, Sn, Cd, Ga), and (Mn, Fe, In), are shown in Fig. 11 a; Co is anti-correlated with (Ag, Cu, Sn, Cd, Ga). On the one hand, high Co, Mn, Fe, and In contents in sphalerite may typify magma-driven hydrothermal systems (i.e., skarn, SEDEX, and VMS deposits, Fig. 11b, c). They are chiefly found in the bottom section of the graph. On the other hand, Ge and Sb tend to be enriched in low-temperature deposits unrelated to a magmatic source (i.e., the Jinding deposit and MVT deposits, Fig. 11b, c). These are located in the top-left section of the plot. Namely, this framework illustrates a positive temperature gradient and differences in metal sources from the top-left to the bottom. The Taolin deposit occupies the middle-bottom-left of the plot, consistent with a medium-low temperature deposition and a main magmatic origin of the ore-forming fluids.

Fig. 15 A sketch profile illustrating the Pb-Zn vein formation at Taolin deposit
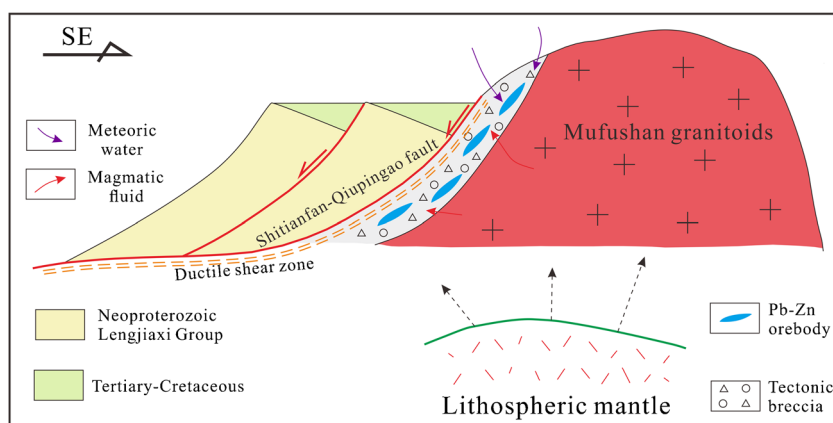
Combined with the results from the trace element compositions of sphalerite and the oxygen-sulfur-lead isotopic components of sulfides, hence, it is reasonable to decipher the Taolin deposit as a medium-low temperature hydrothermal deposit which has genetic relationship with magmatism.

The spatial association of the Taolin deposit with the Mufushan granitoids and the integrated O-S-Pb isotopic components documented by the present study suggest that the Pb-Zn polymetallic mineralization is genetically related to the Mufushan pluton. This is highlighted by that the ore-forming fluids were mainly magmatic water with certain involvement of meteoric water, and that the ore metals were most likely derived from the Mufushan intrusion. In addition, abundant NE- to ENE-trending faults, extensional detachments, emplacement of granitoid plutons, and basin-and-range-like tectonic provinces were well developed in northeastern Hunan Province during Late Jurassic to Cretaceous (Wang et al. 2017; Zou et al. 2018). Accompanying these extension-related structures and voluminous magmatism, large-scale thermal energy probably was generated to facilitate the transportation of fluid flow along the NE–ENE-trending faults (i.e., the Shitianfan-Qiupingao fault) in the northeastern Hunan Province (Fig. 15). Eventually, the gradually decreasing temperature may have been a major cause for ore precipitation and enrichment of the metals in these extensional structures.

Conclusions

(1) The hydrothermal mineralization of the Taolin Pb-Zn deposit can be divided into five stages from early to late, i.e., coarse-grained quartz (stage 1), quartz + fluorite + chlorite + claybank sphalerite (Sp1) + galena + chalcopyrite (stage 2), quartz + barite + fluorite + pale-yellow sphalerite (Sp2) + galena + chalcopyrite (stage 3), quartz with minor chalcopyrite (stage 4), and quartz veinlets (stage 5).

(2) Compared with Sp2, the Sp1 contains higher Fe, Mn, Co, In, and Sn, but lower Ge and Sb. Laser ablation profiles indicate that Fe, Cd, Co, and Mn are mainly present as the solid solution but that Ag, Cu, Pb, Ni, Ga, Ge, Se, Bi, Sb, In, and Sn occur in solid solution or microscopic inclusions. Several substitutions are also discovered: $2Zn^{2+} \leftrightarrow 2(Cu^+, Ag^+) + Ge^{4+}$, $4Zn^{2+} \leftrightarrow 2Sb^{3+} + Pb^{2+} + \square$ (vacancy), $3Zn^{2+} \leftrightarrow In^{3+} + Sn^{3+} + \square$ (vacancy), and $2Zn^{2+} \leftrightarrow (Cu^+, Ag^+) + Sb^{3+}$.

(3) The mineralization temperatures calculated from the sphalerite geothermometer (121 to 292 °C) as well as the ratios of Ga/In (0.96 to 7647) and Zn/Fe (16.32 to 609.7) indicate a medium-low temperature hydrothermal environment for the formation of the Taolin deposit. Besides, with the decreasing Fe and Mn contents of sphalerite from stage 2 (Sp1) to stage 3 (Sp2) of mineralization, the sulfur fugacity increase.

(4) The integrated O-S-Pb isotopic compositions suggest that ore-forming fluids were most likely derived from magmatic water with a minor contribution from meteoric water, and that the ore metals (Pb and Zn) probably derived from the Mufushan intrusion.

(5) Geological features, minor and trace element contents in sphalerite, O-S-Pb isotopic compositions, and PCA results commonly indicate that the Taolin Pb-Zn deposit is a medium-low temperature hydrothermal deposit associated with the magmatism.

References

Bao ZA, Chen L, Zong CL, Yuan HL, Chen KY, Dai MN (2017) Development of pressed sulfide powder tablets for in situ sulfur and lead isotope measurement using LA-MC-ICP-MS. Int J Mass Spectrom 421:255–262

Bauer ME, Burisch M, Ostendorf J, Krause J, Frenzel M, Seifert T, Gutzmer J (2019) Trace element geochemistry of sphalerite in contrasting hydrothermal fluid systems of the Freiberg district, Germany: insights from LA-ICP-MS analysis, near-infrared light microthermometry of sphalerite-hosted fluid inclusions, and sulfur isotope geochemistry. Mineral Deposita 54(2):237–262

Belissont R, Boiron MC, Luais B, Cathelineau M (2014) LA-ICP-MS analyses of minor and trace elements and bulk Ge isotopes in zoned Ge-rich sphalerites from the Noailhac- Saint-Salvy deposit (France): insights into incorporation mechanisms and ore deposition processes. Geochim Cosmochim Acta 126:518–540

Bernardini GP, Borgheresi M, Cipriani C, Di Benedetto F, Romanelli M (2004) Mn distribution in sphalerite: an EPR study. Phys Chem Miner 31(2):80–84

Bonsall TA, Spry PG, Voudouris PC, Tombros S, Seymour KS, Melfos V (2011) The geochemistry of carbonate-replacement Pb-Zn-Ag mineralization in the Lavrion District, Attica, Greece: fluid inclusion, stable isotope, and rare earth element studies. Econ Geol 106(4):619–651

Box SE, Bookstrom AA, Anderson RG (2012) Origins of mineral deposits, Belt-Purcell Basin, United States and Canada: an introduction. Econ Geol 107(6):1081–1088

Cadoux A, Blichert-Toft J, Pinti DL, Fs A (2007) A unique lower mantle source for southern Italy volcanics. Earth Planet Sci Lett 259(3–4):227–238

Cao HW, Zhang ST, Zheng L, Liu RP, Tian HH, Zhang XH, Li JJ (2014) Geochemical characteristics of trace element of sphalerite in the Zhongyuku (Pb)-Zn deposit of the Luanchuan, southwest of China. J Miner Petrology 34(3):50–59 (in Chinese with English abstract)

Catchpole H, Kouzmanov K, Bendezu A, Ovtcharova M, Spikings R, Stein H, Fontbote L (2015) Timing of porphyry (Cu-Mo) and base metal (Zn-Pb-Ag-Cu) mineralisation in a magmatic-hydrothermal system-Morococha district, Peru. Mineral Deposita 50(8):895–922

Charvet J (2013) The Neoproterozoic-Early Paleozoic tectonic evolution of the South China Block: an overview. J Asian Earth Sci 74:198–209

Chen L, Chen KY, Bao ZA, Liang P, Sun TT, Yuan HL (2017) Preparation of standards for in situ sulfur isotope measurement in sulfides using femtosecond laser ablation MC-ICP-MS. J Anal Atom Spectrom 32(1):107–116

Wei C, Huang Z, Yan Z, Hu Y, Ye L (2018a) Trace element contents in sphalerite from the Nayongzhi Zn-Pb deposit, northwestern Guizhou, China: insights into incorporation mechanisms, metallogenic temperature and ore genesis. Minerals 8(11)

Wei C, Ye L, Huang Z, Gao W, Hu Y, Li Z, Zhang J (2018b) Ore genesis and geodynamic setting of Laochang Ag-Pb-Zn-Cu deposit, southern Sanjiang Tethys Metallogenic Belt, China: constraints from whole rock geochemistry, trace elements in sphalerite, zircon U-Pb dating and Pb isotopes. Minerals 8(11)

Cook NJ, Ciobanu CL, Pring A, Skinner W, Shimizu M, Danyushevsky L, Saini-Eidukat B, Melcher F (2009) Trace and minor elements in sphalerite: a LA-ICPMS study. Geochim Cosmochim Acta 73(16):4761–4791

Deng T, Xu D, Chi G, Wang Z, Jiao Q, Ning J, Dong G, Zou F (2017) Geology, geochronology, geochemistry and ore genesis of the Wangu gold deposit in northeastern Hunan Province, Jiangnan Orogen, South China. Ore Geol Rev 88:619–637

Deng T, Xu DR, Chi GX, Zhu YH, Wang ZL, Chen GW, Li ZH, Zhang JL, Ye TW, Yu DS (2019) Revisiting the ca. 845-820-Ma S-type granitic magmatism in the Jiangnan Orogen: new insights on the Neoproterozoic tectono-magmatic evolution of South China. Int Geol Rev 61(4):383–403

Ding TP, Rees CE (1984) The sulfur isotope systematics of the Taolin lead-zinc ore deposit, China. Geochim Cosmochim Acta 48:2381–2392

Ding TP, Younge C, Schwarcz HP (1986) Oxygen, hydrogen, and lead isotope studies of the Taolin lead-zinc ore deposit, China. Econ Geol 81:421–429

Fifarek RH, Rye RO (2005) Stable-isotope geochemistry of the Pierina high-sulfidation Au-Ag deposit, Peru: influence of hydrodynamics on SO2-4-H2S sulfur isotopic exchange in magmatic-steam and steam-heated environments. Chem Geol 215(1–4):253–279

Frenzel M, Hirsch T, Gutzmer J (2016) Gallium, germanium, indium, and other trace and minor elements in sphalerite as a function of deposit type—a meta-analysis. Ore Geol Rev 76:52–78

Fu GG (2009) Ductile shear deformation in northeastern Hunan Province and their constraint on gold mineralization (PhD Degree Thesis). Guangzhou Institute of Geochemistry, Chinese Academy of Sciences, p 123 (in Chinese with English abstract)

Fu ZR, Li XF, Li DW, Wang XD, Wang JC (1991) On ore-controlling of sundry denudational faults. Earth Sci-J China Univ Geosci 16(6):627–634 (in Chinese with English abstract)

Gao LZ, Chen J, Ding XZ, Liu YR, Zhang CH, Zhang H, Liu YX, Pang WH, Zhang YH (2011) Zircon SHRIMP U-Pb dating of the tuff bed of Lengjiaxi and Banxi groups, northeastern Hunan: constraints on the Wuling Movement. Geol Bull China 30(7):1001–1008 (in Chinese with English abstract)

Gao JF, Jackson SE, Dube B, De Souza S (2015) Genesis of the Canadian Malartic, Côté Gold, and Musselwhite gold deposits: insights from LA-ICP-MS element mapping of pyrite. In: Dubé B, Mercier-Langevin P (eds) Targeted geoscience initiative 4: contributions to the understanding of Precambrian lode gold deposits and implications for exploration. Geological Survey of Canada: Open File, p 7852

Gao YB, Li K, Qian B, Li WY, Zheng MC, Zhang CG (2016) Trace elements, S, Pb, He, Ar and C isotopes of sphalerite in the Mayuan Pb-Zn deposit, at the northern margin of the Yangtze plate, China. Acta Petrol Sin 32(1):251–263 (in Chinese with English abstract)

George LL, Cook NJ, Ciobanu CL (2016) Partitioning of trace elements in co-crystallized sphalerite-galena-chalcopyrite hydrothermal ores. Ore Geol Rev 77:97–116

Gomide CS, Brod JA, Junqueira-Brod TC, Buhn BM, Santos RV, Rocha Barbosa ES, Oliveira Cordeiro PF, Palmieri M, Grasso CB, Torres MG (2013) Sulfur isotopes from Brazilian alkaline carbonatite complexes. Chem Geol 341:38–49

Guan YL, Yuan C, Sun M, Wilde S, Long XP, Huang XL, Wang Q (2014) I-type granitoids in the eastern Yangtze Block: implications for the Early Paleozoic intracontinental orogeny in South China. Lithos 206:34–51

Hutchison MN, Scott SD (1983) Experimental calibration of the sphalerite cosmobarometer. Geochim Cosmochim Acta 47(1):101–108

Iwamori H, Albarede F, Nakamura H (2010) Global structure of mantle isotopic heterogeneity and its implications for mantle differentiation and convection. Earth Planet Sci Lett 299(3–4):339–351

Ji WB, Lin W, Faure M, Chen Y, Chu Y, Xue ZH (2017) Origin of the Late Jurassic to Early Cretaceous peraluminous granitoids in the northeastern Hunan province (middle Yangtze region), South China: geodynamic implications for the Paleo-Pacific subduction. J Asian Earth Sci 141:174–193

Jia DC, Hu RZ, Zhao JH, Xie GQ (2003) Lithogeochemical characteristics of the Mesozoic granitic intrusion from the Wangxiang area in

northeastern Hunan Province and its tectonic setting. Acta Geol Sin 77(1):98–103 (in Chinese with English abstract)

Jiang YH, Jiang SY, Dai BZ, Liao SY, Zhao KD, Ling HF (2009) Middle to Late Jurassic felsic and mafic magmatism in southern Hunan Province, southeast China: implications for a continental arc to rifting. Lithos 107(3–4):185–204

Jiao QQ, Wang LX, Deng T, Xu DR, Chen GW, Yu DS, Ye TW, Gao YW (2017) Origin of the ore-forming fluids and metals of the Hetai goldfield in Guangdong Province of South China: constraints from C-H-O-S-Pb-He-Ar isotopes. Ore Geol Rev 88:674–689

Kang B, Yan ZQ, Li LY (2015) Metallogenic model and prospecting criteria of Taolin lead-zinc deposit in Xianglin City, Hunan Province. Resources Environment & Engineering 29(2):160–164 (in Chinese with English abstract)

Keith M, Haase KM, Schwarz-Schampera U, Klemd R, Petersen S, Bach W (2014) Effects of temperature, sulfur, and oxygen fugacity on the composition of sphalerite from submarine hydrothermal vents. Geology 42(8):699–702

Kelly KD, Leach DL, Johnson CA, Clark JL, Fayek M, Slack JF, Anderson VM, Ayuso RA, Ridley WI (2004) Textural, compositional, and sulfur isotope variations of sulfide minerals in the Red Dog Zn-Pb-Ag deposits, Brooks Range, Alaska: implications for ore formation. Econ Geol 99(7):1509–1532

Kissin SA, Mango H (2014) Silver vein deposits. In: Treatise on geochemistry, seconded. Elsevier, Oxford, pp 425–432

Lawley CJM, Richards JP, Anderson RG, Creaser RA, Heaman LM (2010) Geochronology and geochemistry of the MAX porphyry Mo deposit and its relationship to Pb-Zn-Ag mineralization, Kootenay Arc, southeastern British Columbia, Canada. Econ Geol 105(6):1113–1142

Li XF (1992) Lead-zinc-fluorite mineralization associated with denudational faults in Talin ore area, Hunan. Geosci 6(1):46–54 (in Chinese with English abstract)

Li ZX, Li XH (2007) Formation of the 1300-km-wide intracontinental orogen and postorogenic magmatic province in Mesozoic South China: a flat-slab subduction model. Geology 35(2):179–182

Li YB, Liu JM (2006) Calculation of sulfur isotope fractionation in sulfides. Geochim Cosmochim Acta 70(7):1789–1795

Li XF, Yu Y (1991) Lead-zinc mineralization associated with Mufu mountains metamorphic core complex and denudational faulting in the Taolin area, Hunan Province, China. Geotecton Metallog 15(2):90–99 (in Chinese with English abstract)

Li XH, Li ZX, Li WX, Liu Y, Yuan C, Wei GJ, Qi CS (2007) U-Pb zircon, geochemical and Sr-Nd-Hf isotopic constraints on age and origin of Jurassic I- and A-type granites from central Guangdong, SE China: a major igneous event in response to foundering of a subducted flat-slab? Lithos 96:186–204

Li ZK, Li JW, Zhao XF, Zhou MF, Selby D, Bi SJ, Sui JX, Zhao ZJ (2013) Crustal-extension Ag-Pb-Zn veins in the Xiong'ershan district, southern North China Craton: Contraints from the Shagou deposit. Econ Geol 108:1703–1729

Li JH, Zhang YQ, Dong SW, Ma ZL, Li Y (2015) LA-MC-ICPMS zircon U-Pb geochronology of the Hongxiaqiao and Banshanpu Granitoids in eastern Hunan Province and its geological implications. Acta Geosci Sin 36(2):187–196 (in Chinese with English abstract)

Li ZK, Bi SJ, Li JW, Zhang W, Cooke DR, Selby D (2017) Distal Pb-Zn-Ag veins associated with the world-class Donggou porphyry Mo deposit, southern North China craton. Ore Geol Rev 82:232–251

Liu HC, Zhu BQ (1994) Study on the depositional time of the Lengjiaxi Group and Banxi Group in the northwestern Hunan Province. Chin Sci Bull 39(2):148–150 (in Chinese)

Liu YJ, Cao LM, Li ZL, Wang HN, Zhu TQ, Zhang JR (1984) Geochemistry of element. Geological Publishing House, Beijing, pp 1–548 (in Chinese)

Liu TG, Ye L, Zhou JX, Shao SX (2010) The variation of Fe and Cd correlativity in sphalerite with the variation of the mineral color. Geol China 37(5):1457–1468 (in Chinese with English abstract)

Ma Y, Jiang SY, Chen RS, Li XX, Zhu LY, Xiong SF (2019) Hydrothermal evolution and ore genesis of the Zhaiping Ag-Pb-Zn deposit in Fujian Province of Southeast China: evidence from stable isotopes (H, O, C, S) and fluid inclusions. Ore Geol Rev 104:246–265

Murakami H, Ishihara S (2013) Trace elements of indium-bearing sphalerite from tin-polymetallic deposits in Bolivia, China and Japan: a femto-second LA-ICPMS study. Ore Geol Rev 53:223–243

Ohmoto H (1972) Systematics of sulfur and carbon isotopes in hydrothermal ore-deposits. Econ Geol 67(5):551–578

Ohmoto H, Rye RO (1979) Isotopes of sulfur and carbon. In: Barnes, H.L. (Ed.), Geochemistry of Hydrothermal Ore Deposits, second ed. John Wiley and Sons, New York, pp 509–567

Ohmoto H (1986) Stable isotope geochemistry of ore-deposits. Rev Mineral 16:491–559

Roedder E, Howard KW (1988) Taolin Pb-Zn-fluorite deposit, People's Republic of China: an example of some problems in fluid inclusion research on mineral deposits. J Geol Soc Lond 145:163–174

Scott SD, Barnes HL (1971) Sphalerite geothermometry and geobarometry. Econ Geol 66(4):653–669

Seifert T, Sandmann D (2006) Mineralogy and geochemistry of indium-bearing polymetallic vein-type deposits: implications for host minerals from the Freiberg district, eastern Erzgebirge, Germany. Ore Geol Rev 28(1):1–31

Sharp ZD, Gibbons JA, Maltsev O, Atudorei V, Pack A, Sengupta S, Shock EL, Knauth LP (2016) A calibration of the triple oxygen isotope fractionation in the SiO2-H2O system and applications to natural samples. Geochim Cosmochim Acta 186:105–119

Shi HC, Shi XB, Yang XQ, Jiang HY (2013) The exhumation process of Mufushan granite in Jiangnan uplift since Cenozoic: evidence from low-temperature thermochronology. Chinese J Geophys-Ch 56(6):1945–1957 (in Chinese with English abstract)

Shu LS, Wang B, Cawood PA, Santosh M, Xu ZQ (2015) Early Paleozoic and Early Mesozoic intraplate tectonic and magmatic events in the Cathaysia Block, South China. Tectonics 34(8):1600–1621

Sillitoe RH (2010) Porphyry copper systems. Econ Geol 105(1):3–41

Taylor HP (1974) Application of oxygen and hydrogen isotope studies to problems of hydrothermal alteration and ore deposition. Econ Geol 69(6):843–883

Wang QD, Ding BY, Li SJ (1981) Preliminary study on metallogenic temperature characteristics and metallogenic prediction of Taolin lead-zinc deposit, Hunan Province. Journal of Central South Institute of Mining and Metallurgy 1:72–85 (in Chinese)

Wang XL, Zhou JC, Griffin WL, Wang RC, Qiu HS, O'Reilly SY, Xu X, Liu XM, Zhang GL (2007a) Detrital zircon geochronology of Precambrian basement sequences in the Jiangnan orogen: dating the assembly of the Yangtze and Cathaysia blocks. Precambrian Res 159(1–2):117–131

Wang YJ, Fan WM, Sun M, Liang XQ, Zhang YH, Peng TP (2007b) Geochronological, geochemical and geothermal constraints on petrogenesis of the Indosinian peraluminous granites in the South China Block: a case study in the Hunan Province. Lithos 96(3–4):475–502

Wang XL, Zhou JC, Qiu JS, Jiang SY, Shi YR (2008) Geochronology and geochemistry of Neoproterozoic mafic rocks from western Hunan, South China: implications for petrogenesis and post-orogenic extension. Geol Mag 145(2):215–233

Wang W, Wang F, Chen FK, Zhu XY, Xiao P, Siebel W (2010) Detrital zircon ages and Hf-Nd isotopic composition of Neoproterozoic sedimentary rocks in the Yangtze Block: constraints on the deposition age and provenance. J Geol 118(1):79–94

Wang LJ, Yu JH, Griffin WL, O'Reilly SY (2012a) Early crustal evolution in the western Yangtze Block: evidence from U-Pb and Lu-Hf

isotopes on detrital zircons from sedimentary rocks. Precambrian Res 222:368–385

Wang W, Zhou MF, Yan DP, Li JW (2012b) Depositional age, provenance, and tectonic setting of the Neoproterozoic Sibao Group, southeastern Yangtze Block, South China. Precambrian Res 192-95:107–124

Wang D, Wang XL, Zhou JC, Shu XJ (2013a) Unraveling the Precambrian crustal evolution by Neoproterozoic conglomerates, Jiangnan orogen: U-Pb and Hf isotopes of detrital zircons. Precambrian Res 233:223–236

Wang W, Zhou MF, Yan DP, Li L, Malpas J (2013b) Detrital zircon record of Neoproterozoic active-margin sedimentation in the eastern Jiangnan Orogen, South China. Precambrian Res 235:1–19

Wang LX, Ma CQ, Zhang C, Zhang JY, Marks MAW (2014a) Genesis of leucogranite by prolonged fractional crystallization: a case study of the Mufushan complex, South China. Lithos 206:147–163

Wang XL, Zhou JC, Griffin WL, Zhao G, Yu JH, Qiu JS, Zhang YJ, Xing GF (2014b) Geochemical zonation across a Neoproterozoic orogenic belt: isotopic evidence from granitoids and metasedimentary rocks of the Jiangnan orogen, China. Precambrian Res 242:154–171

Wang ZL, Xu DR, Chi GX, Shao YJ, Lai JQ, Deng T, Guo F, Wang Z, Dong GJ, Ning JT, Zou SH (2017) Mineralogical and isotopic constraints on the genesis of the Jingchong Co-Cu polymetallic ore deposit in northeastern Hunan Province, South China. Ore Geol Rev 88:638–654

Wei JX, Ding TP (1984) Study on fluid inclusions and stable isotope of Taolin lead-zinc deposit. Bull Mineral Petrol Geochem 02:40–48 (in Chinese)

Wen ZL, Deng T, Dong GJ, Zou FH, Xu DR, Wang ZL, Lin G, Chen GW (2016) Characteristics of ore-controlling structures of Wangu gold deposit in northeastern Hunan Province. Geotecton Metallog 40(2): 281–294 (in Chinese with English abstract)

Winderbaum L, Ciobanu CL, Cook NJ, Paul M, Metcalfe A, Gilbert S (2012) Multivariate analysis of an LA-ICP-MS trace element dataset for pyrite. Math Geosci 44(7):823–842

Wu G, Chen YC, Li ZY, Liu J, Yang XS, Qiao CJ (2014) Geochronology and fluid inclusion study of the Yinjiagou porphyry-skarn Mo-Cu-pyrite deposit in the East Qinling orogenic belt, China. J Asian Earth Sci 79:585–607

Xu JH, He ZL, Shen SL, Yang ZL, Du JF (1993) Stable isotope geology of the Dongchuang and the Wenyu gold deposits and the source of ore-forming fluids and materials. Contrib Geol Miner Resour Res 8: 87–100 (in Chinese with English abstract)

Xu DR, Chen GW, Xia B, Li PC, He ZL (2006) The Caledonian adakite-like granodiorites in Banshanpu area, eastern Hunan Province, South China: petrogenesis and geological significance. J China Univ Geosci 12(4):507–521 (in Chinese with English abstract)

Xu DR, Gu XX, Li PC, Chen GH, Xia B, Bachlinski R, He ZL, Fu GG (2007) Mesoproterozoic-Neoproterozoic transition: geochemistry, provenance and tectonic setting of clastic sedimentary rocks on the SE margin of the Yangtze Block, South China. J Asian Earth Sci 29(5–6):637–650

Xu DR, Wang L, Li PC, Chen GH, He ZL, Fu GG, Wu J (2009) Petrogenesis of the Lianyunshan granites in northeastern Hunan Province, South China, and its geodynamic implications. Acta Petrol Sin 25(5):1056–1078 (in Chinese with English abstract)

Xu DR, Deng T, Chi GX, Wang ZL, Zou FH, Zhang JL, Zou SH (2017) Gold mineralization in the Jiangnan Orogenic Belt of South China: geological, geochemical and geochronological characteristics, ore deposit-type and geodynamic setting. Ore Geol Rev 88:565–618

Yang Q, Xia XP, Zhang WF, Zhang YQ, Xiong BQ, Xu YG, Wang Q, Wei GJ (2018) An evaluation of precision and accuracy of SIMS oxygen isotope analysis. Solid Earth Sci 3:81–86

Yao JL, Shu LS, Santosh M, Zhao GC (2014) Neoproterozoic arc-related mafic-ultramafic rocks and syn-collision granite from the western segment of the Jiangnan Orogen, South China: constraints on the

Neoproterozoic assembly of the Yangtze and Cathaysia blocks. Precambrian Res 243:39–62

Ye L, Cook NJ, Ciobanu CL, Liu YP, Zhang Q, Liu TG, Gao W, Yang YL, Danyushevskiy L (2011) Trace and minor elements in sphalerite from base metal deposits in South China: a LA-ICPMS study. Ore Geol Rev 39(4):188–217

Ye L, Gao W, Yang YL, Liu TG, Peng SS (2012) Trace elements in sphalerite in Laochang Pb-Zn polymetallic deposit, Lancang, Yunnan Province. Acta Petrol Sin 28 (5):1362–1372

Yu AN (1993) Studies on fault system, metallogenetic age and model of Taolin Pb-Zn deposit in Hunan Province. Geol Explor Non-ferrous Metals 2(1):39–46 (in Chinese with English abstract)

Yu AN, Ye BL (1998) The affirmation of Dayunshan metamorphic core complex structure and its origin. Hunan Geol 17(2):81–84 (in Chinese with English abstract)

Yu QH, Li RQ, Feng ZT (1987) The typomorphic characteristics of sphalerite from the lead-zinc deposits in Nanling area. Proceedings of the first national symposium on mineralogy, Geological Publishing House, Beijing, 80–85 (in Chinese)

Yu AN, Ye BL, Peng ES (1998) Relationship between the Dayunshan metamorphic core complex and mineralization, Taolin, Hunan Province. Geotecton Metallog 22(1):82–88 (in Chinese with English abstract)

Yuan B, Zhang CQ, Yu HJ, Yang YM, Zhao YX, Zhu CC, Ding QF, Zhou YB, Yang JC, Xu Y (2018a) Element enrichment characteristics: insights from element geochemistry of sphalerite in Daliangzi Pb-Zn deposit, Sichuan, Southwest China. J Geochem Explor 186:187–201

Yuan HL, Liu X, Chen L, Bao ZA, Chen KY, Zong CL, Li XC, Qiu JW (2018b) Simultaneous measurement of sulfur and lead isotopes in sulfides using nanosecond laser ablation coupled with two multi-collector inductively coupled plasma mass spectrometers. J Asian Earth Sci 154:386–396

Zhao GC, Cawood PA (2012) Precambrian geology of China. Precambrian Res 222:13-54

Zartman RE, Doe BR (1981) Plumbotectonics—the model. Tectonophysics 75:135–162

Zhai DG, Liu JJ, Zhang HY, Tombros S, Zhang AL (2018) A magmatic-hydrothermal origin for Ag-Pb-Zn vein formation at the Bianjiadayuan deposit, inner Mongolia, NE China: evidences from fluid inclusion, stable (C-H-O) and noble gas isotope studies. Ore Geol Rev 101:1–16

Zhai DG, Liu JJ, Cook NJ, Wang XL, Yang YQ, Zhang AL, Jiao YC (2019) Mineralogical, textural, sulfur and lead isotope constraints on the origin of Ag-Pb-Zn mineralization at Bianjiadayuan, Inner Mongolia, NE China. Mineral Deposita 54(1):47–66

Zhang JL (1989) On the ore-controlling condition and metallogenic prognosis of the Taolin Pb-Zn deposit, Hunan. Geol Prospect 25(4):1–7 (in Chinese with English abstract)

Zhang JL, Fu CM (1987) Reapproach of metallogeny and controlling condition of Taolin lead-zinc ore deposit, Linxiang County. Hunan Geol 6:14–22 (in Chinese with English abstract)

Zhang SB, Zheng YF (2013) Formation and evolution of Precambrian continental lithosphere in South China. Gondwana Res 23(4):1241–1260

Zhang YZ, Wang YJ, Fan WM, Zhang AM, Ma LY (2012) Geochronological and geochemical constraints on the metasomatised source for the Neoproterozoic (similar to 825 Ma) high-mg volcanic rocks from the Cangshuipu area (Hunan Province) along the Jiangnan domain and their tectonic implications. Precambrian Res 220:139–157

Zhao GC (2015) Jiangnan Orogen in South China: developing from divergent double subduction. Gondwana Res 27(3):1173–1180

Zhao JS, Qiu XL, Zhao B, Tu XL, Yu J, Lu TS (2007) REE geochemistry of mineralized skarns from Daye to Wushan region, China. Geochim 36(4):400–412 (in Chinese with English abstract)

Zhou MF, Yan DP, Kennedy AK, Li YQ, Ding J (2002) SHRIMP U-Pb zircon geochronological and geochemical evidence for Neoproterozoic arc-magmatism along the western margin of the Yangtze Block, South China. Earth Planet Sci Lett 196(1–2):51–67

Zhou XM, Sun T, Shen WZ, Shu LS, Niu YL (2006) Petrogenesis of Mesozoic granitoids and volcanic rocks in South China: a response to tectonic evolution. Episodes 29(1):26–33

Zhou JC, Wang XL, Qiu JS (2009) Geochronology of Neoproterozoic mafic rocks and sandstones from northeastern Guizhou, South China: coeval arc magmatism and sedimentation. Precambrian Res 170(1–2):27–42

Zhao GC, Cawood PA (2012) Precambrian geology of China. Precambrian Res 222:13–54

Zhu KY, Li ZX, Xu XS, Wilde SA (2014) A Mesozoic Andean-type orogenic cycle in southeastern China as recorded by granitoid evolution. Am J Sci 314(1):187–234

Zhuang LL, Song YC, Liu YC, Fard M, Hou ZQ (2019) Major and trace elements and sulfur isotopes in two stages of sphalerite from the world-class Angouran Zn-Pb deposit, Iran: implications for mineralization conditions and type. Ore Geol Rev 109:184–200

Zou ZG (1993) Study of mineralogic characteristics of sphalerite from Taolin, Hunan. Hunan Geol 12(2):102–108 (in Chinese with English abstract)

Zou ZC, Hu RZ, Bi XW, Ye L, Wu LY, Feng CX, Tang YY (2012) Trace element geochemistry of the Liziping Pb-Zn deposit,the Lanping Basin,Northwest Yunnan Province,China. Geochim 41(5):482–496 (in Chinese with English abstract)

Zou SH, Zou FH, Ning JT, Deng T, Yu DS, Ye TW, Xu DR, Wang ZL (2018) A stand-alone Co mineral deposit in northeastern Hunan Province, South China: its timing, origin of ore fluids and metal Co, and geodynamic setting. Ore Geol Rev 92:42–60